A HIGHLY ASYMMETRIC HYBRID DIRECTIONAL COUPLER SENSOR

by

Can Sümer

A Thesis Submitted to the
Graduate School of Engineering and Natural Sciences
In Partial Fulfillment of the Requirements for
The Degree of

Master of Science

Sabancı University
Spring 2005

A HIGHLY ASYMMETRIC HYBRID DIRECTIONAL COUPLER SENSOR

Can Sümer

APPROVED BY:

Assist. Prof. Dr. Cem Öztürk …………………………….

(Thesis Supervisor)

Assoc. Prof. Dr. Meriç Özcan …………………………….

Assist. Prof. Dr. Cleva Ow-Yang …………………………….

DATE OF APPROVAL: 16 / 08 / 2005

© Can Sümer 2005

All Rights Reserved

Dedicated to those

Who stand firm

And hold their light

High and proud

~

In loving memory of

Ümit Ballı

Kemal Sümer

Yaşar Aktuğ

ABSTRACT

A HIGHLY ASYMMETRIC HYBRID DIRECTIONAL COUPLER SENSOR

Can Sümer

The advances in the microelectronics industry and microfabrication techniques in the past few decades have lead to an increase in the capabilities and features of all kinds of sensors. From pressure sensors to chemical sensors, all kinds of devices have gone through fundamental improvements, giving rise to a generation of sensors with better quality, higher precision and lower cost and power consumption.

In this work, a new optical chemical sensor was designed. The structure is based on a highly asymmetric directional coupler, where the asymmetry implies a high refractive index difference between the core layers of the waveguides in the coupler, rather than an asymmetry in the geometry.

The device designed presents a very high sensitivity to both the operating wavelength, and the index of refraction of the target material. Therefore, monitoring can be performed in two alternative ways, namely, by monitoring the output power at a specified wavelength of operation, or by monitoring the whole multi-wavelength spectrum for a changing refractive index. The coupler is composed of a polymer ridge waveguide and a semiconductor slab waveguide.

Fabricating the sensor employs conventional microelectronic fabrication techniques and can easily be integrated with various microelectronic components. The complete top-down fabrication scheme for the devices is presented, giving specific recipes and techniques. The materials to be used in the fabrication are selected to yield the best results in the device performance. Also, fabrication processes for each individual layer are optimized in order to obtain the desired device structure.

ÖZET

YÜKSEK DERECEDE ASİMETRİK MELEZ YÖN BAĞLAŞTIRICI ALGILAYICI

Can Sümer

Geçtiğimiz yıllarda mikroelektronik endüstrisinde ve mikroüretim tekniklerinde olan ilerlemeler tüm algılayıcı türlerinin kapasite ve özelliklerinde bir artışa yol açmıştır. Basınç algılayıcılarından kimyasal algılayıcılara, bütün aygıtlar esaslı bir gelişme sürecinden geçmiş, bu da daha kaliteli, daha hassas, daha ucuz ve daha az güç tüketimli bir algılayıcılar nesline yol açmıştır.

Bu çalışmada, yeni bir optik kimyasal algılayıcı tasarlanmıştır. Yapı, yüksek derecede asimetrik bir yön bağlaştırıcı üzerine kuruludur ve asimetri geometrideki bir asimetriden ziyade, bağlaştırıcıdaki dalga rehberlerinin iç nüve bölgelerinin kırılma indisleri arasındaki bir asimetriyi ifade etmektedir.

Tasarlanan aygıt hem çalıştırma dalgaboyuna hem de hedef malzemenin kırılma indisine karşı yüksek bir hassasiyet göstermektedir. Böylelikle, denetleme belli bir çalıştırma dalgaboyundaki çıkış gücünün denetlenmesi, ya da değişken bir kırılma indisi için bütün çoklu-dalgaboyu tayfının denetlenmesi olarak iki ayrı şekile gerçekleştirilebilmektedir. Bağlaştırıcı, bir polimer kabartma çizgi dalga rehberi ve bir yarıiletken dilim dalga rehberinden oluşmaktadır.

Algılayıcı modern mikroelektronik üretim teknikleriyle üretilebilmektedir ve kolaylıkla çeşitli mikroelektronik bileşenlerle tümlenebilir. Aygıtlar için baştan sona tam üretim planı belirli tarif ve teknikler verilerek sunulmuştur. Üretimde kullanılacak malzemeler aygıt başarımı açısından en iyi sonuçları verecek şekilde seçilmiştir. Ek olarak, her bir katmanın üretim süreçleri, istenen aygıt yapısını elde edebilmek için mükemmele eriştirilmiştir.

ACKNOWLEDGEMENTS

I would like to express my sincere gratitude to my thesis advisor Dr. Cem Öztürk for his extensive support, encouragement, inspiration and above all, for his patience and his faith in me throughout the past two years. He has been the major driving force in my studies, and it has been an invaluable experience being his student and working with him.

I would like to thank professors of Faculty of Engineering and Natural Sciences, Dr. Cleva Ow-Yang and Dr. Meriç Özcan for taking part in my thesis committee, and also Dr. Yaşar Gürbüz, Dr. Ayhan Bozkurt, Dr. Mehmet Ali Gülgün, Dr. Naci Inci, Dr. İsmet İnönü Kaya and Dr. Ersin Göğüş for their inspirations, support and guidance.

Faculty personnel and our Laboratory Technician Bülent Köroğlu deserves a special appreciation for he has taught me how to use each and every machine and tool in the Cleanroom Lab and I would like to thank him for being a great coach and for his patience.

Dr. Mehdi Farmanesh deserves a special mention for his continuous support, guidance and sincere interest in my studies throughout my academic life. I would like to thank him for he has inspired me to the field of Microelectronics and without him none of these would be possible.

I would like to thank my friends Akın Ünal, Özgür Taşdizen and Atilla Özgür Çakmak for being the best office mates anyone could have; Emre Heves for the four elements found in the nature; İstem Özen for sharing the idealism; Yalçın Yamaner for the critical data; Nusrettin Güleç for the late night talks; Arda of Café Dorm for the late night meals; Bora Bekiroğlu for the music; Emrah Kavlak for the kebabs, Aslı Narin for all the laughs and photographs; Umut Gülmez and the Eskişehir gang for holding the light and all the drinks together; Efe Kafdağlı and Emre Gürdamar for sticking with me for all these years; Emre Yiğit Kızılırmak for the housing support, Fevzi Ballı for showing

me distances do not matter; each and every member of the White Russian Band, Sezen Aksu Choir Band, Keşf-i Kadim, and The Fellowship: Ate, Boru, Rune and Topçu, and all of the above for bringing me joy, keeping me alive and always being there for me.

Thanks would never be enough for my dear friends and mentors Birol Gökduman and Betül Duru Gökduman, for they have advanced at the forefront and lead the way for those who follow.

I would like to thank Deniz Gizem Öztürk for she has gone through this whole journey by my side and her support was with me every single day of this effort.

Last, but certainly not least, I would like to thank my mom, my dad and my sister. Thank you for letting me make all of my choices in my life with my free will. None of these would be possible without you.

TABLE OF CONTENTS

ABSTRACT .... **v**

ÖZET .... **vi**

ACKNOWLEDGEMENTS .... **vii**

LIST OF FIGURES .... **xii**

LIST OF TABLES .... **xiv**

CHAPTER 1 - INTRODUCTION **1**

1.1. Introduction 1

1.2. Sensors 1

1.2.1. Electrical Sensors 2

1.2.2. Quartz Crystal Microbalance (QCM) Sensors 2

1.2.3. Surface Acoustic-Wave (SAW) Sensors 3

1.3. Optical Sensors 4

1.3.1. Fiber-Optic Chemical Sensors 4

1.3.2. Optical Surface Plasmon Resonance (SPR) Sensors 5

1.3.3. Optical Waveguide Sensors 5

1.4. Highly Asymmetric Hybrid Directional Coupler Sensor 6

1.5. Thesis Flow 6

CHAPTER 2 - DEVICE FUNDAMENTALS **7**

2.1. Introduction 7

2.2. Wavelength Dependence of Asymmetric Directional Couplers 7

2.3. Asymmetric Directional Coupler for Sensor Applications 13

2.4. Proposed Device Structure 13

2.4.1. Polymer Ridge Waveguide 14
2.4.2. Semiconductor Slab Waveguide 16
2.4.3. Hybrid Sensor 17
2.5. Polymer – Semiconductor Hybrid Structure 19

CHAPTER 3 - SIMULATIONS AND RESULTS 23
3.1. Introduction 23
3.2. Simulation Method 23
3.3. Simulation Sets and Results 25
3.3.1. Simulation Set #1 25
3.3.2. Simulation Set #2 30
3.3.3. Simulation Set #3 32
3.3.4. Simulation Set #4 35
3.3.5. Simulation Set #5 37
3.4. Simulations Summary and Discussion 40
3.4.1. A Blood Glucose Sensor 41

CHAPTER 4 - DEVICE FABRICATION 44
4.1. Introduction 44
4.2. Materials and Processes 44
4.2.1. Fabrication of BCB Layers 44
4.2.2. Fabrication of PDBCB Layer 46
4.2.3. Fabrication of Semiconductor Layer 48
4.2.4. Fabrication of Ridge Structure – Reactive Ion Etching of BCB 49
4.3. Overall Process Flow 49

CHAPTER 5 - CONCLUSIONS AND FUTURE WORK 55
5.1. Conclusions 55
5.2. Future Work 56

APPENDIX A - BRIEF INVESTIGATION OF THICKNESS DEPENDENCE OF THE WAVELENGTH OF OPERATION 57
A.1. Introduction 57
A.2. Simulation Method and Results 57

APPENDIX B - BRIEF ANALYSIS OF THE SYMMETRIC DIRECTIONAL COUPLER 59

B.1. Introduction 59

B.2. Simulation Method 59

B.3. Simulations and Results 59

REFERENCES 63

LIST OF FIGURES

2-1: A generic directional coupler structure. 8
2-2: Polymer ridge waveguide. 14
2-3: The guiding principle of a generic ridge waveguide – 2-D effective index approximation. 15
2-4: The measured refractive indices of BCB and PDBCB [27]. 16
2-5: Semiconductor slab waveguide. 17
2-6: Generic hybrid waveguide sensor structure. 18
3-1: 3-D illustration of the device and the y-branch scheme. 24
3-2: Asymmetric directional coupler sensor configuration #1. 25
3-3: Output power vs. n_{out} for configuration #1. 26
3-4: Output power vs. n_{out} for configuration #1 when the common cladding thickness is increased to 10 μm. 27
3-5: Output power vs. n_{out} for configuration #1 when the fourth mode is of interest in the semiconductor slab guide. 28
3-6: Output power vs. wavelength of operation for configuration #1 for n_{out} = 1.3330 and n_{out} =1.3344. 29
3-7: Output power vs. wavelength of operation for configuration #1 29
3-8: Asymmetric directional coupler sensor configuration #2. 30
3-9: Output power vs. n_{out} for configuration #2. 31
3-10: Output power vs. wavelength of operation for configuration #2. 31
3-11: Output power vs. wavelength of operation for configuration #2 for n_{out} = 1.5000 and n_{out} = 1.5014. 32
3-12: Asymmetric directional coupler sensor configuration #3. 33
3-13: Output power vs. n_{out} for configuration #3. 34
3-14: Output power vs. wavelength of operation for configuration #3. 34
3-15: Output power vs. wavelength of operation for configuration #3 for n_{out} = 1.3330 and n_{out} = 1.3344. 35

3-16: Asymmetric directional coupler sensor configuration #4. 35
3-17: Output power vs. n_{out} for configuration #4. 36
3-18: Output power vs. wavelength of operation for configuration #4 for n_{out} = 1.5000 and n_{out} =1.5014. 37
3-19: Asymmetric directional coupler sensor configuration #5. 38
3-20: Output power vs. n_{out} for configuration #5. 38
3-21: Output power vs. wavelength of operation for configuration #5 for n_{out} = 1.3330 and n_{out} = 1.3344. 39
3-22: Normalized output of configuration #3 with respect to normal human blood refractive index. 42
3-23: Normalized output of configuration #3 with respect to normal human blood glucose level. 42
4-1: Ratio of the polymerized BCB with respect to curing duration and temperature for the full cure process. 46
4-2: Fabrication step #1 – spin-coat and partial cure of BCB. 50
4-3: Fabrication step #2 – reactive ion etching of BCB. 51
4-4: Fabrication step #3 – spin-coat, exposure, developing. 52
4-5: Fabrication step #4 – spin-coat of BCB and full cure. 53
4-6: Final step of fabrication – thin-film deposition of the silicon layer. 54
A-1: Device structure for thickness-dependence analysis 57
A-2: Wavelength of mode-matching vs. semiconductor layer thickness 58
B-1: Symmetric directional coupler sensor configuration. 60
B-2: Output power vs. n_{out} for the symmetric device. 60
B-3: Comparison of n_{out} dependences of symmetric and asymmetric configurations. ... 61
B-4: Output power vs. wavelength of operation for symmetric configuration for n_{out} = 1.5000 and n_{out} =1.5014. 62
B-5: Comparison of multi-wavelength spectrums of symmetric and asymmetric configurations. 62

LIST OF TABLES

3-1: Summary of the general properties of simulated sensor configurations. 40
4-1: Recommended soft bake temperatures with respect to pre-bake PDBCB thicknesses, for a given soft bake time of 90 seconds. 47

CHAPTER 1

INTRODUCTION

1.1. Introduction

The advances in the microelectronics industry and microfabrication techniques in the past few decades have lead to an increase in the capabilities and features of all kinds of sensors. New sensing applications and new sensing techniques can be realized. From pressure sensors to chemical sensors, all kinds of devices have gone through fundamental improvements, giving rise to a generation of sensors with better quality, higher precision and lower cost and power consumption.

The purpose of this work is to propose a new optical sensor for detecting the chemical concentrations in various materials like blood. Our motivation is the increasing connection and interaction between the technology and humankind. The integration of optical technologies and the semiconductor technologies is another important goal in this work.

1.2. Sensors

A sensor is a device or a biological organ that detects or senses a signal, a physical condition, a chemical compound, or a change in a local environment. The human body contains many types of sensors, which are specialized cells sensitive to light, motion, temperature, sound, toxins, nutrients, glucose level, oxygen level, hormones, neurotransmitters, proteins, etc. The technological sensors, which can also be defined as transducers that convert a quantity or a parameter into a signal carrying information, also come in a great variety and function. According to the nature of the signal carrying the information, a sensor can be characterized as electrical, mechanical

or optical. On the other hand, sensors are also classified according to the parameter to be measured (e.g. the stimulus) as mechanical (position, acceleration, flow rate, etc), thermal (temperature, etc), electrostatic, magnetic, radiation (electromagnetic, nuclear, etc), chemical (humidity, gases, ions, etc), and biological (enzymes, antigens, antibodies, etc) sensors. In addition, another type of classification is according to the type of response, which leads to physical sensors, chemical sensors and biosensors. Since the sensor structure to be proposed in this work is a chemical one, it is worthwhile to investigate the types of chemical sensors, in the sense of the interaction forming the base of operation.

1.2.1. Electrical Sensors

Electrical sensors operate on the basis of the response being a change in electrical signal. Their principle of operation is detecting changes in current, voltage, power or etc. In the case of detecting a chemical or a gas in the environment, they mostly work on the principle of change in the conductivity or resistivity. The main idea is the use of materials sensitive to selected chemicals as individual components. [1], [2], or in specific layers which are sensitive to certain chemicals, in devices like Schottky diodes and MOSFETS, enabling various gases like Hydrogen [3], NH_3, Ethanol, and H_2S [4] to be detected. The operating principle of the electrical sensors in chemical detection is as follows: depending on the concentration of the substance to be detected in the ambient, some of the material in the medium is either absorbed from or emitted into the ambient by the sensitive layer. As a result of this process, the electrical resistivity and/or the conductivity of the layer changes, and consequently, the electrical properties of the entire device will change.

These types of sensors enable fabrication of the sensor structure itself and the readout circuitry in the same processing steps. In addition, the sensor structure and the readout circuitry being adjacent reduces the overall size of the device and allows the system to be more compact.

1.2.2. Quartz Crystal Microbalance (QCM) Sensors

The quartz crystal microbalance (QCM) sensors are a relatively simple kind of piezoelectric sensors capable of measuring temperature, pressure, force, acceleration, and also mass changes in the case of chemical sensing. QCM sensors consist of a few-millimeter thick resonating disk with metal electrodes on each side. The basic principle

of operation is as follows: When excited with the oscillating signal, device goes into a resonance state at a characteristic frequency. The resonating disk is preferably coated with an active sensing material to provide the sensing operation. When the device is exposed to the medium where the target material is present, then the adsorption of the chemical causes an increase of mass in the resonating disk. This leads to a decrease in the resonance frequency, and sensing can be achieved by measuring the change in the resonance frequency. Mass changes to a resolution of 1 picogram have been reported [5].

The QCM sensors have the advantage of being highly linear over a wide range, and their sensitivity to temperature changes is relatively low. It is possible to change the target material by simply changing the coating of the resonant disk, and hence the device structure is generic [6].

The operation of the QCM sensors may experience some size-dependent issues. When the overall dimensions of the device are on the order of a micron, the surface-to-volume ratios increase, and the noise in the device becomes an issue because of kinetics-limited surface processes causing instabilities. Signal-to-noise ratio of QCM sensors decreases with increasing surface-to-volume, and hence the accuracy of the device decreases. Also, in the case of repetitive measurements, a recovery time or a reference medium is generally necessary in order to have accurate results. Recovery times up to tens of seconds have been reported [7].

1.2.3. Surface Acoustic-Wave (SAW) Sensors

The surface acoustic-wave (SAW) sensors are similar to QCM devices; however, they differ in some important points. First of all, in SAW devices, a surface wave travels over the surface of the device instead of throughout its volume. Also, SAW sensors operate at much higher frequencies than the QCM sensors and hence they can generate a larger change in the frequency [5]. The SAW devices are usually made of a relatively thick plate of piezoelectric materials like zinc oxide or lithium niobate, with electrodes to excite the oscillation of the surface wave. The surface acoustic-wave is stimulated by applying an oscillatory signal to the fingers of the electrode to cause a deformation in the surface. Subsequent propagation of the surface wave is determined by the changes in the properties of the surface material. In a common gas sensors using SAW device with a multiple structures, the sensing arms are coated with a sensitive material, while a single arm is left out acting as a reference in order to reduce the effect of factors like temperature and so on [8].

Since the SAW sensors use the surface wave in their principle of operation, the device structure is planar, and therefore the device can be fabricated by photolithographic methods. As in the case of QCMs, it is possible to change the target material of a SAW sensor by simply changing the coating of the sensitive membrane, and hence the device structure is generic [5]. On the other hand, both QCM and SAW sensors share a common disadvantage that, both sensors require more complex peripheral electronics compared to electrical sensors. Also, both structures require frequency detectors, whose resonant frequencies may drift as the active membrane ages [5].

1.3. Optical Sensors

Optical sensing is another mechanism available for chemical sensors. As in the case of electrical and acoustic sensors, there are several kinds of optical sensors present, used in a variety of areas from biomedical sensing to environmental monitoring [9].

1.3.1. Fiber-Optic Chemical Sensors

One class of optical chemical sensors is the fiber-optic chemical sensor, where the sensor structure is based on the advantageous properties of the optical fiber technology. Optical fiber technology presents many advantages over the electrical methods. First of all, optical fibers present a very low loss figure over long distances, typically less than 0.2 dB/kilometer. Moreover, optical fibers are immune to electromagnetic interference, and they produce no electromagnetic radiation like the electrical transmission lines. In addition, signals carried within the optical fibers can be very low in power, usually in the range of milli Watts [10].

A technique for using optical fibers in chemical sensors is the coating of porous layers on the fiber substrate. In this technique, diffusion of the target material into the porous layer coated around the fiber is detected by induced change of optical properties such as the refractive index, optical absorption, or fluorescence. These changes cause a shift in the amplitude or the phase (or both) of the optical wave traveling in the optical fiber, which can be detected at the output of the fiber, and hence forms the principle of operation for the fiber-optic chemical sensors [11-13].

1.3.2. Optical Surface Plasmon Resonance (SPR) Sensors

Another class of optical sensors used in chemical sensing is the optical surface plasmon resonance (SPR) sensor, in which the sensing mechanism is based on the optical phenomenon called surface plasmon resonance. Surface plasmon resonance is achieved by optically exciting a standing charge density wave at the interface between a thin dielectric and a metal surface [14]. The conditions for exciting the charge density and the performance of the surface plasmon resonance are determined by the angle and the energy of the incident photon, the complex dielectric constant of the metal, the refractive index of the substrate on which the metal is deposited, and changes in the refractive index of the sample at the metal surface [14]. Applications of optical SPR sensors, which are sensitive to the change of the refractive index on the surface of a sample, have been reported for various purposes over the past years [14-16].

1.3.3. Optical Waveguide Sensors

Optical waveguide structures are extensively used in chemical sensing applications. Various methods have been used in sensing mechanisms employing optical waveguides to detect several chemicals, gases, vapors or humidity. The principle of operation of the optical waveguide sensors is related to internal reflection spectroscopy, and it takes the advantage that light will propagate through a medium by internal reflection [17]. The lightwave can interact with a second material, which is in contact with the reflecting surface of this medium. The degree of interaction is related to the angle and wavelength of the incident light and the refractive indices of the two media. If the refractive indices of the waveguide and the coating media are close to each other, then the lightwave is not reflected at the interface, but travels without interference into the second media. If light is absorbed as it passes through the structure, then the waveguide can be used for spectroscopic analyses. The more reflections that occur, the greater the degree of interaction of the lightwave with the structure. The sensitivity of the device is thus a function of the length and the thickness of the waveguide [17]. Abundant examples are available in the literature, employing different waveguide structures for several sensing applications [17-23].

1.4. Highly Asymmetric Hybrid Directional Coupler Sensor

The device to be presented in this work is a Highly Asymmetric Hybrid Directional Coupler Sensor, which is a chemical sensor based on an optical asymmetric directional coupler structure. The sensing mechanism is based on the critical matching between the waveguides in the coupler structure. This matching highly depends on both the refractive indices of the waveguides employed in the structure, and the wavelength of operation. This yields not only a very high, but also a two-fold sensitivity on the sensor performance. While the changes in the refractive index of a layer in the structure can be measured via the change of output power at any given wavelength, the change can also be measured via the investigation of the multi-wavelength spectrum of the output.

The materials of choice and the fabrication methods of the structure also make the integration of the device with existing IC and microelectronic technologies possible. The fabrication of the device involves standard semiconductor process technologies and introduces no extra cost.

1.5. Thesis Flow

The rest of this work is laid down as follows. The second chapter discusses the fundamentals of directional couplers and introduces the proposed device to be investigated in this work. The third chapter outlines the expected characteristics of the device and includes detailed investigations and simulations of the device operation. The fourth chapter discusses the fabrication of the proposed device. It includes the material properties and the fabrication methods for the materials to be used in the structure. Furthermore, the fourth chapter also includes a top-down fabrication recipe for the proposed device. Finally, the fifth chapter summarizes the work done and concludes the written part of this work. It discusses the insights gained and the results obtained, and also proposes the next steps in the future work.

CHAPTER 2

DEVICE FUNDAMENTALS

2.1. Introduction

This chapter introduces the proposed device in this work and presents its fundamental working principles. The proposed structure is a highly asymmetric directional coupler, where the asymmetry implies the difference in the refractive index dispersions of the modes, instead of an asymmetry in the geometry of the device. The device operation is highly-wavelength dependent as will be shown, and the structure can be utilized for sensor applications, and easily integrated in standard semiconductor technologies. The basic device operation stems from the fact that a refractive index change within a layer of a directional coupler causes a change in the power spectrum, allowing for changes in the refractive index to be monitored by a change in power.

In this chapter, the structure and the properties of the proposed device structure will be presented. How the structure can be utilized in sensor applications will be discussed. Following the sensor approach, the wavelength-dependent operation of the device and the degree of wavelength dependency will be investigated.

2.2. Wavelength Dependence of Asymmetric Directional Couplers

A directional coupler consists of two co-directional waveguides. In order to correctly simulate the above described hybrid structure, the light input and output through the device is restricted to one waveguide. A method to analyze such a topology is to use the perturbation theory, i.e., to derive the propagation behavior of the incident mode throughout the structure. This leads to viewing the presence of the second waveguide as a perturbation to the effective index solution for the modes for the main

waveguide of interest. According to this approach, the total field at any point throughout the structure is expressed using the individual unperturbed effective index solution for the modes of separate waveguides. If we assume weak coupling, the solution of this approach is the coupled-mode equations. The weak-coupling assumption will be discussed later. The figure below shows a generic directional coupler structure in order to assist the further discussions.

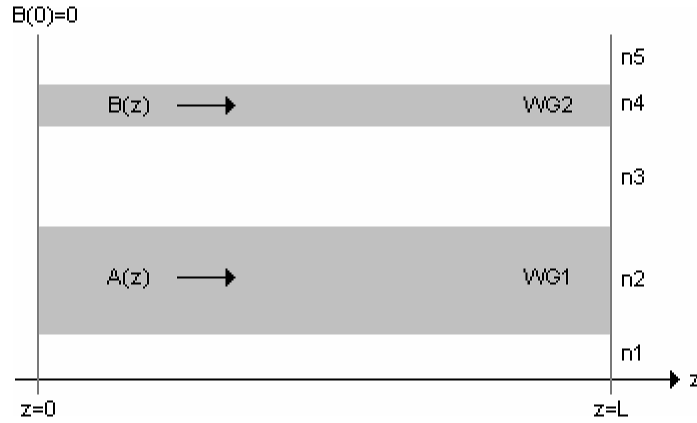

Figure 2-1: A generic directional coupler structure.

If we assume that $U_1(x,y)$ and $U_2(x,y)$ are the unperturbed eigenfunction solutions and, β_1 and β_2 are the unperturbed eigenvalue solutions to the wave equation for the two individual waveguides, the solutions of co-directional couplers ($\beta_1 > 0$, $\beta_2 > 0$) are in the form [24]:

$$A(z) = \left[a_1 e^{j\beta_0 z} + a_2 e^{-j\beta_0 z}\right]\exp(-j\delta z), \qquad (2.2\text{-}1a)$$

$$B(z) = \left[b_1 e^{j\beta_0 z} + b_2 e^{-j\beta_0 z}\right]\exp(j\delta z), \qquad (2.2\text{-}1b)$$

where,

$$\delta = \frac{|\beta_2 - \beta_1|}{2}, \qquad (2.2\text{-}2)$$

and

$$\beta_0^{\ 2} = \delta^2 + \kappa^2. \qquad (2.2\text{-}3)$$

In the equations above, δ represents the difference in the effective propagation constants for separate waveguide modes, and is known as the detuning parameter; meanwhile, κ represents the amount of mode overlap between the two waveguide modes, and is known as the coupling coefficient. κ can be represented using the perturbation analysis as [25]:

$$\kappa^2 = \kappa_{1,2}\kappa_{2,1} \tag{2.2-4}$$

where,

$$\kappa_{i,j} = \frac{k_0^{\ 2}}{2\beta_i}\frac{\iint_{WG_i} \Delta\varepsilon_i U_i^*(x,y)U_j(x,y)dxdy}{\iint \left|U_i^*(x,y)\right|dxdy}. \tag{2.2-5}$$

Constants a_1, a_2, b_1, and b_2 should satisfy the following initial conditions:

$$a_1 + a_2 = A(0), \tag{2.2-6a}$$

$$b_1 + b_2 = B(0). \tag{2.2-6b}$$

Substituting Equations (2.2-1) into the coupled mode Equations written as [24]:

$$\frac{dA}{dz} = -j\kappa_{1,2}B\exp[-j(\beta_2-\beta_1)z], \tag{2.2-7a}$$

$$\frac{dB}{dz} = -j\kappa_{2,1}A\exp[j(\beta_2-\beta_1)z], \tag{2.2-7b}$$

And applying the initial conditions of Equations (2.2-6), we obtain:

$$A(z) = \left\{\left[\cos(\beta_0 z) + i\frac{\delta}{\beta_0}\sin(\beta_0 z)\right]A(0) - i\frac{\kappa}{\beta_0}\sin(\beta_0 z)B(0)\right\}e^{-i\delta z}, \tag{2.2-8a}$$

$$B(z) = \left\{-i\frac{\kappa}{\beta_0}\sin(\beta_0 z)A(0) + \left[\cos(\beta_0 z) - i\frac{\delta}{\beta_0}\sin(\beta_0 z)\right]B(0)\right\}e^{-i\delta z}. \tag{2.2-8b}$$

Then, introducing the initial condition of the field at the input of the second waveguide being equal to zero ($B(0) = 0$), we can write the field amplitudes at any given point of the structure as follows [26]:

$$\beta_0 A(z) = A(0)\left[\cos(\beta_0 z) - i\delta \sin(\beta_0 z)\right]e^{-i\delta z}, \tag{2.2-9a}$$

$$\beta_0 B(z) = -iA(0)\kappa \sin(\beta_0 z)e^{-i\delta z}. \tag{2.2-9b}$$

We see from the above coupled-mode Equations (2.2-9) that the maximum power transfer from the first waveguide to the second waveguide takes place for $\beta_0 L_c = \frac{\pi}{2}$. The length L_c seen in this equation is referred to as the coupling length for the directional coupler. At the coupling length, the amount of power transferred from the first waveguide to the second waveguide can be expressed as [27]:

$$\frac{\left|B(L_c)^2\right|}{\left|A(0)^2\right|} = \frac{1}{\left(\frac{\delta^2}{\kappa^2} + 1\right)}. \tag{2.2-10}$$

We see from the above Equation (2.2-10) that the coupling of power from one waveguide to the other depends not only on the amount of mode overlap, but also on the propagation constants of both waveguide modes.

At the phase-matching condition [26], $\beta_1 = \beta_2$ and hence $\delta = 0$; as a result, at the coupling length $L = \frac{\pi}{2\kappa}$, all of the power in the first waveguide is transferred to the second waveguide for all wavelengths of operation. For the symmetric case, the coupling coefficient κ, representing the amount of mode overlap between the two waveguide modes, usually changes negligibly with respect to wavelength, and therefore it can be taken as constant. Here, it should be reminded that $\beta_1$and β_2 are the unperturbed eigenvalue solutions to the wave equation for the two individual waveguides.

For the asymmetric case, the resultant effective index solutions for the modes for the two waveguides in the device lead to different effective index dispersions.

Nevertheless, the two waveguides in the structure can be designed such that the effective index solutions for the modes of these waveguides can match exactly at a certain wavelength. At this specific wavelength, the operation of the asymmetric coupler turns out to be similar to the operation of the symmetric case. In addition, even though the refractive index dispersion curves for the two waveguides in the structure are usually different from each other, the curves will meet at the wavelength specified above. What is more, the tangential slopes of the dispersion curves also turn out to be different, and this leads to a fast increase in the detuning parameter for the wavelengths away from the wavelength where the effective indices match. Remembering that the maximum power that can be transferred to the second waveguide depends strongly on the detuning parameter, we conclude that the coupling between the waveguides will also be limited at the wavelengths away from the mode matching wavelength.

Since the coupling between the waveguides in the coupler is dependent on the operating wavelength, it is obvious that the amount of wavelength dependence is due to $\frac{\partial \Delta\beta}{\partial \lambda}$, which is the differential dispersion of the detuning parameter [27]. Thus, in order to have effective wavelength selectivity using an asymmetric directional coupler, we must employ two waveguides in the structure whose effective index dispersion curves are different from each other, but at the same time, these curves must intersect at a single point, i.e., at a single wavelength. Here, it is implied that merely a difference in the effective indices values of the cores is an insufficient condition, but also a difference in the dispersions is required.

To illustrate the refractive index sensitivity of the critical coupling, consider the specific example involving the case when $\delta = \kappa$, which leads to the amount of power transferred from the first waveguide to the second waveguide at a coupling length being equal to *50 %* of the input power. Then, considering

$$\delta = \frac{2\pi\Delta n}{\lambda}, \tag{2.2-11}$$

and taking the coupling coefficient κ to be 10^{-1} (which is a very high ratio of coupling), and the operating wavelength to be 1.55 μm, we get an approximate refractive index change of:

$$\Delta n \approx 2.46 \times 10^{-4} . \qquad (2.2\text{-}12)$$

Thinking "backwards" in the above set of example calculations, we can point out that, even if there is a very small effective index change between to modes in the order of 10^{-4}, then the amount of power coupled from one waveguide to the other will be affected in the order of *50 %*. This shows that the sensitivity of the structure to the refractive index changes is in fact, very high.

Then, revisiting the generic coupler structure in Fig. 2-1 in the light of the above discussion, we see that, if the refractive indices n_1 and n_5 are smaller than n_3, and if the refractive index of the second (top) core layer, n_4, is much greater than that of the first (bottom) core layer, where an index difference larger than 1 will suffice; the absolute cut-off of the highest order modes of both waveguides will be at n_3. To express mathematically, the condition is where,

$$n_1, n_5 \le n_3 \qquad (2.2\text{-}13)$$

and

$$n_4 >> n_2 \qquad (2.2\text{-}14)$$

where,

$$n_4 - n_2 > 1 \qquad (2.2\text{-}15)$$

Under these conditions, since n_3 is the common cladding, it is possible to satisfy $\beta_1=\beta_2$ at any wavelength, as previously shown [27]. Also, in the simplest terms, since the relative refractive index dispersion will be in the limits from n_2 to n_3 in the first waveguide and from n_4 to n_3 in the second waveguide, as long as n_4 is much greater than n_2, it is obvious that the dispersions will be significantly different from each other. This fact has been shown by Ozturk, et al., [27] and will also be shown in the following sections of this work with examples, and hence a mathematical proof is not necessary in the scope of this work. Here, we conclude that, as the asymmetry in the coupler structure increases, we get higher wavelength dependency in the operation.

2.3. Asymmetric Directional Coupler for Sensor Applications

Returning to the coupled mode analysis, we can investigate the asymmetric directional coupler structure using an unperturbed analysis, i.e., we can investigate the solutions of the wave equations for the two separate waveguides without taking into account the effect of the other waveguide.

A change in the refractive index of the upper layer, n_5, should lead to change in β and $\beta(\lambda)$ values, which causes a $\Delta\beta$ amount of change in the tuning parameters. Hence, since a refractive index change causes a change in the maximum output power, the change in n_5 is measurable.

This structure has the advantage of allowing two separate ways of measuring the change in n_5, as a result of the above investigation. First, a change in the refractive index n_5 can be measured via the change of output power at any given wavelength. Or, the change can be measured via the investigation of the multi-wavelength spectrum of the output. Both of these measurement methods will be shown with examples in the following chapter.

2.4. Proposed Device Structure

Prior to proposing a device structure for the work, it is worthwhile to outline the main expected properties and requirements of the structure. Using the above terminology, the first waveguide, which will be both the input and the output of the coupler structure, should be a low loss structure and have an effective refractive index close the fiber delivering the power in and out. Also the mode profile of the structure should match the fiber mode profile as highly as possible. In addition, the device should be realizable with conventional semiconductor and microfabrication process technologies, and be compatible with integration in the previously mentioned technologies.

For the second waveguide structure, a semiconductor waveguide is chosen due to several reasons. First of all, the index of most semiconductors is much higher relatively than that of the fiber, and since our first guide has indices close to that of fiver, a high asymmetry is guaranteed. Also, integration with the semiconductor and microfabrication technologies is essential as described above. For the second waveguide,

silicon and gallium arsenide is expected to meet the requirements of the structure, due to their well known processability and refractive index properties.

The device proposed in this work is the combination of a polymer ridge waveguide and a semiconductor slab waveguide, which share a common cladding region. The resulting device is a hybrid highly asymmetric directional coupler. A structure similar to the one to be investigated here was previously presented by Ozturk [27], and this work follows his studies on the device fundamentals. In order to come to a complete model of the device structure, the individual waveguides can be considered first separately (unperturbed analysis), and then in an estimation of the overall device working principles.

2.4.1. Polymer Ridge Waveguide

The ridge waveguide to be considered in this work is an all-polymer ridge waveguide with BCB polymer (benzocyclobutene) as the core and PDBCB (Photo-definable benzocyclobutene) polymer used as the cladding regions. Detailed analyses of these two materials are given later in this thesis, in Chapter 4 on Device Fabrication. For the purposes of this chapter, the knowledge of the relative refractive indices of these materials, that the refractive index of PDBCB is slightly higher than that of BCB, and that both indices are approximately 1.535 at the wavelength of 1.55 μm, will be sufficient. This gives us the symmetric ridge waveguide structure illustrated in Fig. 2-2, where the refractive indices of the core and the cladding regions are given as n_1 and n_2, respectively. The guiding principle of the ridge waveguide is well known [26, 28, 29], and a summary obtained using the 2-D effective index approximation follows [27]:

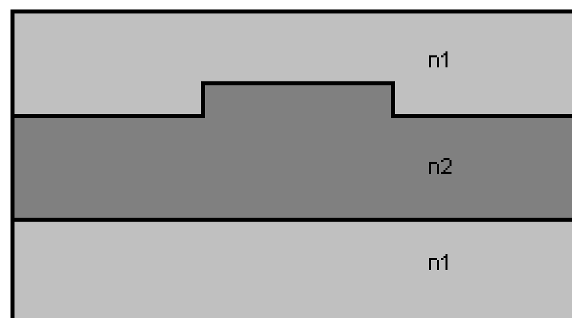

Figure 2-2: Polymer ridge waveguide.

In the ridge waveguide structure depicted above, n_2 is slightly greater than n_1, which makes the vertical guiding of the mode apparent. According to the 2-D effective

index approximation, assuming no variations throughout the lateral direction, the three regions A, B and C defined in Fig. 2-3 can be considered individually. Then what we have as a result is three layer slab waveguide, whose dimensions and layer indices are defined according to the original ridge waveguide, also depicted in Fig. 2-3:

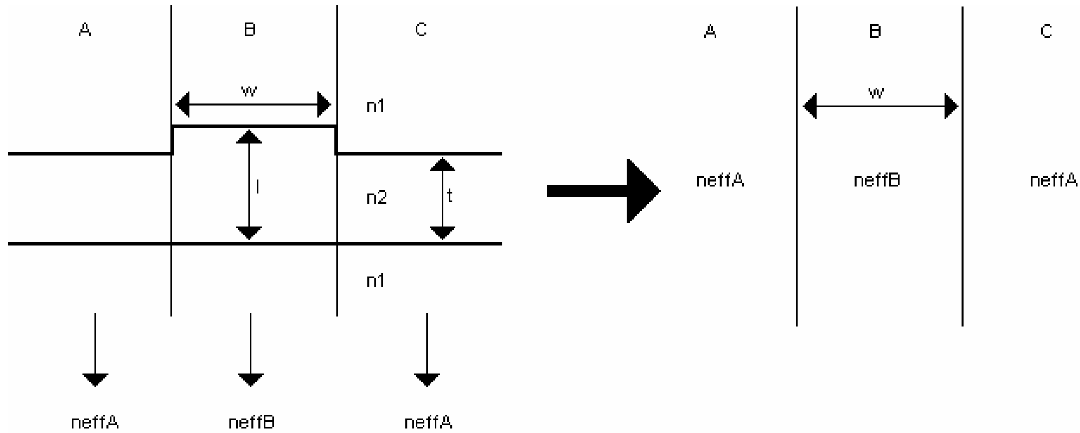

Figure 2-3: The guiding principle of a generic ridge waveguide – 2-D effective index approximation.

In the resultant structure, what we have in region A (and region C) is a three slab waveguide with a core thickness equal to t. If t is chosen (using 2-D effective index approximation) such that the slab waveguide is single-mode, then it follows that $n_1 < n_{eff\text{-}A} < n_2$ [27]. Similarly, in region B, what we have is again a three slab waveguide with a core thickness equal to l. Likewise, if l is chosen such that the slab waveguide is single-mode, then it follows that $n_1 < n_{eff\text{-}B} < n_2$, and also $n_{eff\text{-}B} > n_{eff\text{-}A}$ since it is given in the generic ridge structure that $l > t$. Once the vertical slabs are defined and set to be single-mode, then the analysis in the vertical direction is simply the solution of a three layer slab waveguide, with a core thickness of w. Like the previous slab solutions, if the w is chosen such that the slab waveguide is single-mode, then the single-mode guiding of the whole structure is guaranteed.

In order to make sure that the layers in the ridge waveguide satisfy the single mode conditions, the respective (and relative) refractive indices of the individual materials must be known. The indices can be obtained by spectroscopic ellipsometry [27]. When performed for a wavelength spectrum of 1 μm to 1.6 μm, the measurements result in the index dispersions illustrated in the Fig. 2-4 [1]:

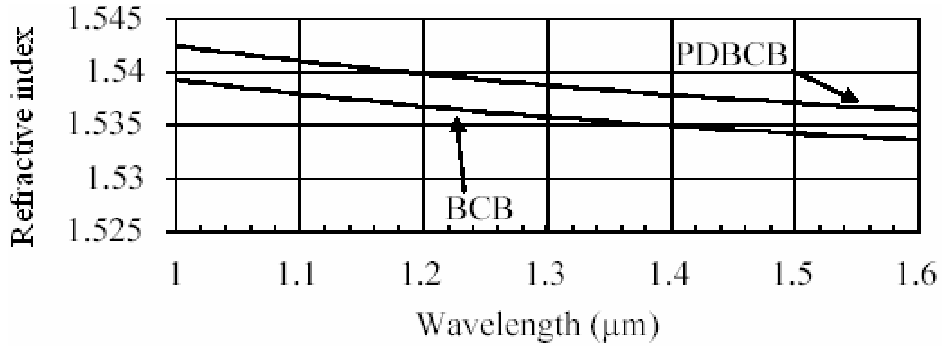

Figure 2-4: The measured refractive indices of BCB and PDBCB [27].

What is more, the characteristics depicted in Figure 2-4 can be approximated with high precision by the following function for BCB:

$$n_{BCB}(\lambda) = (1.528493) + \frac{(0.014508)}{\lambda^2} - \frac{(0.003716)}{\lambda^4}, \tag{2.4-1}$$

and by the following function for PDBCB [27]:

$$n_{PDBCB}(\lambda) = (1.530907) + \frac{(0.015802)}{\lambda^2} - \frac{(0.004267)}{\lambda^4}. \tag{2.4-2}$$

Using the above formulation, the refractive index of BCB and PDBCB are obtained to be 1.534 and 1.537 respectively, at the wavelength of 1.55 μm. The 0.003 difference between the relative refractive indices of the two materials give rise to the possibility of creating a waveguide structure, depicted previously in Fig. 2-2.

2.4.2. Semiconductor Slab Waveguide

The second waveguide structure within the device is a semiconductor slab guide, which consists of the shared cladding region with the ridge waveguide, a semiconductor guiding layer and another cladding region, which also forms the outer region of the overall device. The overall slab waveguide structure is illustrated in Fig. 2-5:

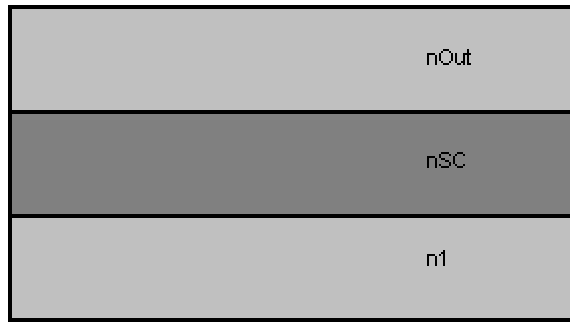

Figure 2-5: Semiconductor slab waveguide.

The working principles of this asymmetric slab waveguide are also well known [26, 28, 29], and the guiding mechanism is based on the refractive index difference between the core and the cladding regions. Unlike the polymer waveguide, the indices of the cladding regions are asymmetric, in other words, they are not the same. Also, the difference between the indices of the core and the cladding regions are higher with respect to the difference in the polymer guide, i.e., the index of the common cladding, semiconductor, and the outer layers being around 1.534, 3.37 and 1.33, respectively, at a wavelength of 1.55 μm.

2.4.3. Hybrid Sensor

The overall device, as described at the beginning of this chapter, is the combination of the two waveguide structures described above, with the BCB cladding region being the common cladding region. The overall device structure is shown below, in Fig. 2-6:

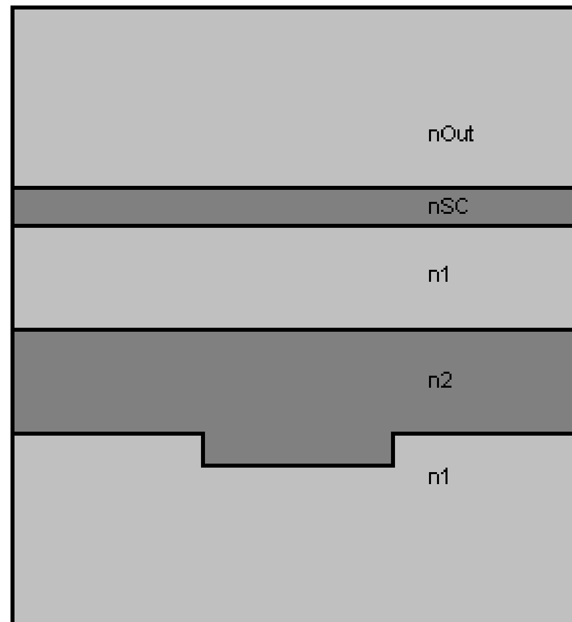

Figure 2-6: Generic hybrid waveguide sensor structure.

The overall device structure is a highly asymmetric (due to the asymmetry in the refractive indices) directional coupler and the coupling between the waveguides depends on the operating wavelength [30]. The polymer part of the device is the polymer waveguide described previously, and the semiconductor part is the semiconductor waveguide described in the above section. The upper cladding of the polymer waveguide, namely the BCB layer in the middle of the device, is where the two structures meet, and this layer is used as the cladding for both waveguides. In the device definition, the substrate is neglected since it is not a crucial part of the design and does not affect the device performance as long as the lower BCB cladding is sufficiently thick, i.e., its thickness "goes to infinity" in terms of the device parameters and calculations.

The wavelength-dependent properties of this whole structure have been analyzed by Ozturk, et al. [27]. In the work of Ozturk, et al., the semiconductor waveguide has been realized in the structure of a p-i-n diode, and in this way the core refractive index of the second waveguide has been changed electronically and the wavelength-dependence of the structure was investigated. In our work, on the other hand, the effect of the outer medium effective index on the wavelength-dependence was investigated. Note that, although this structure have been investigated using the above structure, this particular device realizes a generic idea for the asymmetric directional couplers. It should be added that, in realizing this generic idea, in terms of both the physical

constraints like fiber-to-waveguide coupling and a low-loss condition, and the wavelength constraints, the optimum results and performance are expected to be obtained using this proposed structure.

2.5. Polymer – Semiconductor Hybrid Structure

In light of the discussions above, we see that the structure fits the definitions and properties of an asymmetric directional coupler. The two waveguides in the structure are the polymer waveguide and the semiconductor waveguide. Considering that the refractive indices of the core layer materials are around 1.5 (n_{BCB}) and around 3.4 (n_{SC}) at a wavelength of 1.55 μm, it seems unlikely we can achieve any coupling with this structure. However, when inspected further, coupling is in fact possible due to two facts. First, the common BCB cladding layer in the middle section of the structure is shared by both waveguides. And second, the silicon or gallium arsenide slab waveguide is generally a multi-mode structure. Since the semiconductor guide has the BCB cladding, the highest-order mode of this guide must have an effective refractive index that is close to the refractive index of BCB. Therefore, for the suggested semiconductor slab waveguide structure, the effective refractive index of the highest-order guided mode must match the effective refractive index of the single-mode polymer waveguide perfectly [31]. In addition, due to the high refractive index of silicon (or gallium arsenide), the refractive index dispersion curve of the highest mode of the slab waveguide is expected to be significantly different than the dispersion curve of the polymer ridge guide, and this leads to that the coupling will vastly depend on the operating wavelength.

Then, the next task is to show that the suggested generic device in fact fits the above described asymmetric directional coupler fundamentals; that is to show that the mode-matching can occur and to mathematically estimate the precise spectral position where the mode-matching for an hybrid structure occurs. Using a 1-D analysis is both sufficient and practical in this task for not only the analytical solutions are already available, but also the complexity of the 2-D analysis which lacks any advantage over the 1-D analysis in this approach. The refractive index solutions of the modes are necessary to investigate the spectral characteristics of the coupling, and a 1-D analytical solution is sufficient for this purpose.

Both waveguides can be treated as slab waveguides in the transverse direction.

The polymer waveguide can be treated as a symmetric slab waveguide with PDBCB in the core layer and BCB as the cladding layers. The semiconductor waveguide can be treated as an asymmetric slab waveguide with BCB in the lower cladding and n_{out} in the upper cladding. Then, the effective index solution to the slab waveguides has the form of the known general characteristic equations [26]:

$$\frac{2\pi}{\lambda} t \sqrt{n_{core}^2 - n_{eff}^2} - \tan^{-1}(h) - \tan^{-1}(q) = m\pi\,, \qquad (2.5\text{-}1)$$

where,

$$h = \frac{\sqrt{n_{core}^2 - n_{bottom}^2}}{\sqrt{n_{core}^2 - n_{eff}^2}}\,, \qquad (2.5\text{-}2a)$$

$$q = \frac{\sqrt{n_{core}^2 - n_{upper}^2}}{\sqrt{n_{core}^2 - n_{eff}^2}}\,, \qquad (2.5\text{-}2b)$$

for TE polarization and,

$$h = \frac{\sqrt{n_{core}^2 - n_{bottom}^2}}{\sqrt{n_{core}^2 - n_{eff}^2}} * \frac{n_{core}^2}{n_{bottom}^2} \qquad (2.5\text{-}3a)$$

$$q = \frac{\sqrt{n_{core}^2 - n_{upper}^2}}{\sqrt{n_{core}^2 - n_{eff}^2}} * \frac{n_{core}^2}{n_{upper}^2}\,, \qquad (2.5\text{-}3b)$$

for TM polarization. In the above characteristic equation, λ is the wavelength of operation, t is the physical thickness of the core of the slab waveguide, n_{eff} is the effective refractive index of the guided mode, and m is the transverse mode number.

It is obvious that m should be equal to 1 for the polymer waveguide, since the structure is designed to be single-mode in the wavelength spectrum of interest. Then, for the polymer waveguide to be used in the structure, we can fix the effective refractive index dispersion, which will be the solution to the characteristic waveguide equation in the form $n_{BCB}(\lambda) < n_{eff,poly}(\lambda) < n_{PDBCB}(\lambda)$.

It can be seen from the characteristic equation that the effective index solutions depend strongly in the thickness of the semiconductor layer (First term of Equation 2.5-1). Since the thickness of the semiconductor layer depends on the process parameters, as will be explained in Chapter 4 on Device Fabrication, it is controllable and becomes the primary design parameter for achieving mode matching at a certain wavelength. The mode-matching condition is satisfied when the effective refractive index of the semiconductor waveguide equals that of the polymer waveguide at a specific wavelength of operation. Then, putting in the values to be used in the structure, the characteristic equation for the mode matching condition can be expressed as:

$$\frac{2\pi}{\lambda} t_{SC} \sqrt{\left(n_{SC}(\lambda)\right)^2 - \left(n_{eff,poly}(\lambda)\right)^2} - \tan^{-1}(h) - \tan^{-1}(q) = m\pi , \qquad (2.5\text{-}4)$$

where,

$$h = \frac{\sqrt{\left(n_{SC}(\lambda)\right)^2 - \left(n_{BCB}(\lambda)\right)^2}}{\sqrt{\left(n_{SC}(\lambda)\right)^2 - \left(n_{eff,poly}(\lambda)\right)^2}} \qquad (2.5\text{-}5a)$$

$$q = \frac{\sqrt{\left(n_{SC}(\lambda)\right)^2 - \left(n_{out}(\lambda)\right)^2}}{\sqrt{\left(n_{SC}(\lambda)\right)^2 - \left(n_{eff,poly}(\lambda)\right)^2}} \qquad (2.5\text{-}5b)$$

for TE polarization and,

$$h = \frac{\sqrt{\left(n_{SC}(\lambda)\right)^2 - \left(n_{BCB}(\lambda)\right)^2}}{\sqrt{\left(n_{SC}(\lambda)\right)^2 - \left(n_{eff,poly}(\lambda)\right)^2}} * \frac{\left(n_{SC}(\lambda)\right)^2}{\left(n_{BCB}(\lambda)\right)^2} \qquad (2.5\text{-}6a)$$

$$q = \frac{\sqrt{\left(n_{SC}(\lambda)\right)^2 - \left(n_{out}(\lambda)\right)^2}}{\sqrt{\left(n_{SC}(\lambda)\right)^2 - \left(n_{eff,poly}(\lambda)\right)^2}} * \frac{\left(n_{SC}(\lambda)\right)^2}{\left(n_{out}(\lambda)\right)^2} \qquad (2.5\text{-}6b)$$

for TM polarization. Then, knowing the refractive indices of the layers and the wavelength of operation, the thickness of the semiconductor layer (t_{SC}) becomes the primary design parameter. To achieve critical coupling for a specific wavelength, the characteristic equation for the mode matching condition must be solved in order to obtain the primary design parameter t_{SC}.

It can be seen from the above equations that there will be multiple solutions to the thickness t_{SC} depending on the mode number m (index-matching will be obtained for the highest-order mode supported in the multi-mode waveguide), and also it can be seen that the solutions for the TE and TM modes will be different. In addition, the effective index birefringence does not exist for the polymer waveguide since

$$n_{BCB}(\lambda) < n_{eff,poly}(\lambda) < n_{PDBCB}(\lambda), \qquad (2.5\text{-}7)$$

and the two polymers used in the structure have a refractive index difference around 0.003 for the wavelength range of interest. However, for the semiconductor guide, due to the high refractive index difference between the core and the cladding regions, and also between the core and the outer region, the boundary conditions are different for different polarizations. This leads to very different refractive index dispersion solutions for TE and TM modes for the semiconductor slab mode. As a result, the coupling condition is expected to be polarization dependent.

So, our simulation results should demonstrate that, for a specific supported number of modes and a specific polarization in the slab guide, there will be a certain thickness t_{SC} to guarantee critical mode matching at a predetermined, very narrow wavelength window, and mode matching will not prevail for the wavelengths even slightly away from the predetermined center wavelength.

CHAPTER 3

SIMULATIONS AND RESULTS

3.1. Introduction

Following the device fundamentals presented in the previous chapter, the simulation methodology for the proposed generic device structure will be presented here, as well as an extensive collection of results obtained together with the performance analysis.

3.2. Simulation Method

The simulations in this work are performed using the derivations presented in the previous chapter and the calculations are performed using MATLAB. The simulation methodology used is as follows: As stated in the previous chapter, both waveguides can be treated as slab waveguides in the transverse direction. The polymer waveguide can be treated as a symmetric slab waveguide with PDBCB in the core layer and BCB as the cladding layers. The semiconductor waveguide can be treated as an asymmetric slab waveguide with BCB in the lower cladding and n_{out} in the upper cladding. The resulting equations were given previously, together with the fact that the primary design parameter being t_{SC}, thickness of the core layer of the semiconductor slab waveguide. Then, the methodology employing the unperturbed analysis is to find the effective refractive index of the polymer guide, and then to compute the corresponding t_{SC} to match the effective index of the semiconductor slab guide at a certain wavelength. When all the indices and the operating wavelength are known for this specific case, the mode matching condition is satisfied. Then, the overall performance and the transmission spectrum are calculated using the supermode theory. The performance

analysis performed on the device aims to investigate the effects of:

- Semiconductor slab thickness (number of modes supported),
- Sensing medium,
- Common cladding thickness.

The "output" to be monitored will be the power at the output of the polymer waveguide. Because, adopting the analysis from the previous chapter, the polymer waveguide is the "first" waveguide in the structure, and hence it is thought of as the input to the device, and also as the output. To clarify the relation further, the device can be thought of as placed in a y-branch scheme, half the light power input to the polymer waveguide in the asymmetric directional coupler device, and half the light power going straight to the read-out peripherals, as the reference. It should be noted that, when calculating the power ratios between the input and the output, the input power will be taken as the whole power instead of this 50 percent, in other words, the ratios will be normalized. This scheme is illustrated in the following figure, together with a 3-D illustration of the device:

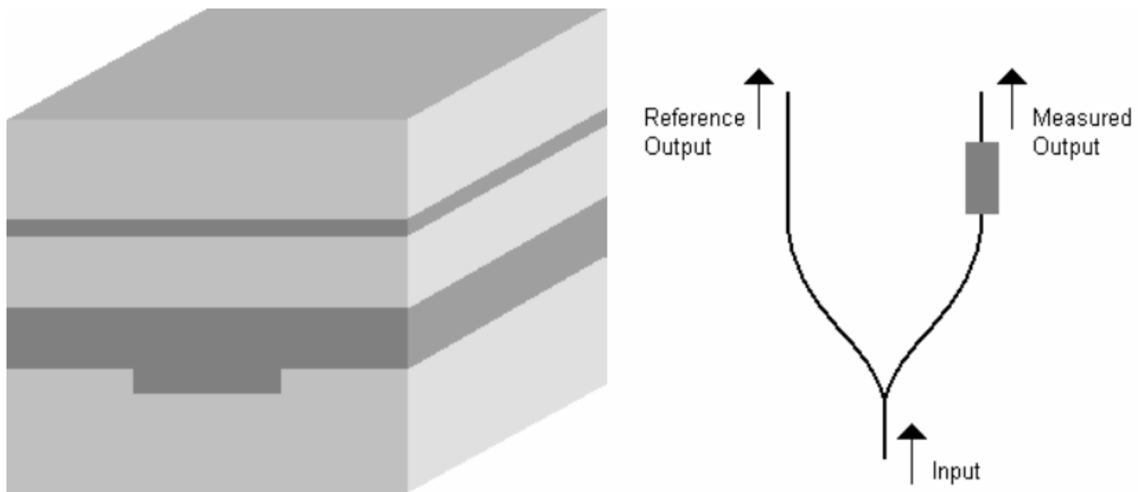

Figure 3-1: 3-D illustration of the device and the y-branch scheme.

In addition, it should be noted that, as previously mentioned, the measurements are possible in two ways in the system, one being the measurement of the power at the output as described above, and the other being the measurement of the whole multi-wavelength spectrum.

3.3. Simulation Sets and Results

Illustrating the methodology with the first of the simulation sets shall clarify the technique used in the simulations. The verbal descriptions of the basic methods will be limited to the first set only; however, additional information will be given whenever necessary.

3.3.1. Simulation Set #1

Let's start with the initial set, which employs the device configuration illustrated in the following figure:

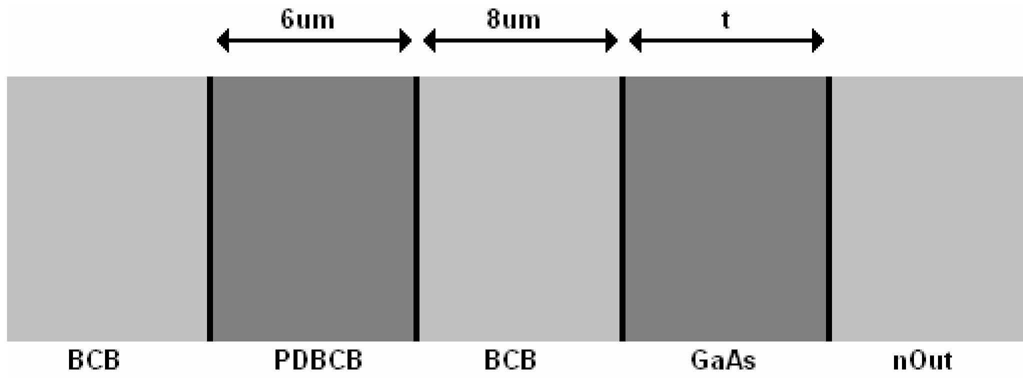

Figure 3-2: Asymmetric directional coupler sensor configuration #1.

As seen in the figure, the device to be investigated is an asymmetric directional coupler, with the core thickness of the polymer layer set as 6 µm, and the thickness of the common cladding set as 8 µm. For the semiconductor guide, Gallium Arsenide, which has a refractive index around 3.376, is selected for the core. The refractive index of the outer layer is set to be n_{out} = 1.3330, for the initial case. For an operating wavelength of 1.55 µm, the refractive indices of the polymers are $n_{BCB}(1.55) = 1.533887$ and $n_{PDBCB}(1.55) = 1.536745$.

With these figures, the effective index of the polymer slab waveguide is calculated using the 1-D effective index method as $n_{eff,poly}(1.55) = 1.535349$, which satisfies the relation

$$n_{BCB}(\lambda) < n_{eff,poly}(\lambda) < n_{PDBCB}(\lambda), \qquad (3.3\text{-}1)$$

as expected. Then, if the core thickness of the semiconductor waveguide is selected

such that the effective indices of both waveguides match, then critical coupling can be achieved. The way to do this is to iterate the 1-D effective index solution “backwards” for the semiconductor waveguide, and hence come to a solution for the thickness t_{SC}. It should be noted that all the values obtained with this method are re-checked with the “forward” 1-D effective index method and verified.

Using this method, the thickness of the core layer is found to be t = 279.842 nm, when the mode number m equals 1, meaning that *the second mode is of interest* in the semiconductor slab guide. In all the structures to be discussed in this work, the mode number m is 0 for the polymer guides, since the polymer waveguide is fundamentally designed to be a single-mode structure.

At this point, where the primary design parameter t_{SC} is obtained, what is achieved is that, an asymmetric directional coupler is designed with the mode matching condition satisfied for a determined and a specific condition. What follows is investigation of the effects of parameters like n_{out}, mode number m, thickness of the common cladding on the mode matching condition, and to investigate the multi-wavelength characteristics of the device. Here, it should be noted that the all of power calculations are performed for a device-length equal to the coupling length L_c, which is in the order of less then 10 mm [27]. Investigating the n_{out} dependence of this configuration, when the output power is calculated with respect to the outer layer refractive index, the following figure is obtained:

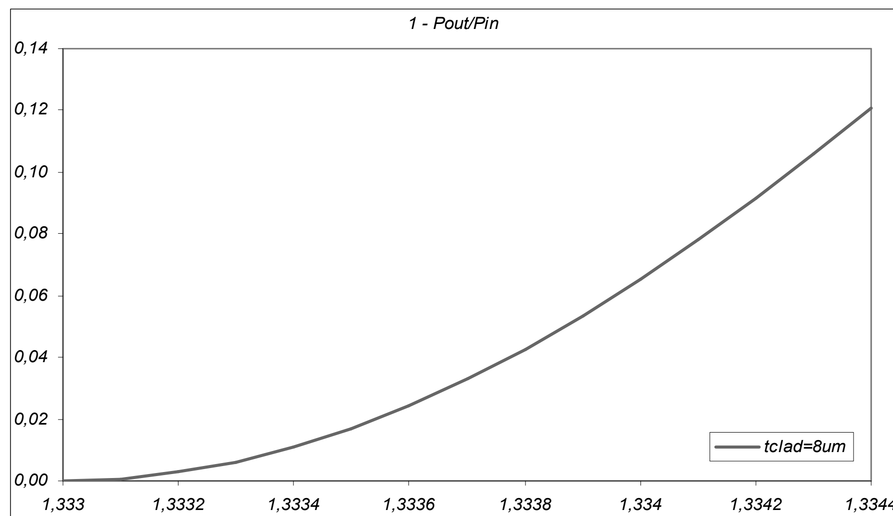

Figure 3-3: Output power vs. n_{out} for configuration #1.

We see from the above graph that, all of the input power is coupled to the second

waveguide when the outer layer refractive index equals 1.3330, whereas, as the outer refractive index increases, the amount of power at the output increases, and 12% of the input power is seen at the output as n_{out} reaches the value of 1.3344 [32, 33].

Moreover, when the thickness of the common cladding region is increased, we see that the amount of power seen at the output increases by the order of more than 2 when the outer layer refractive index equals 1.3344, and this is shown in the following figure, together with the previous result:

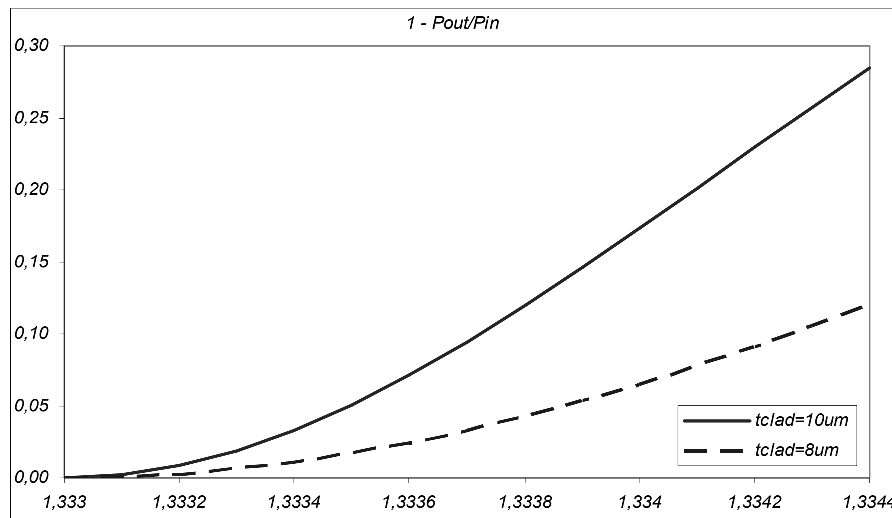

Figure 3-4: Output power vs. n_{out} for configuration #1 when the common cladding thickness is increased to 10 μm.

It can be seen from the above figure that as the thickness of the common cladding region increases, the amount of power coupled to the second waveguide will decrease as the refractive index of the outer layer increases. However, there is a physical limit to the thickness of the common cladding layer, because even though the calculations show the chance of the critical matching condition, coupling will not be possible beyond a certain thickness as this thickness “goes to infinity” in terms of device parameters and calculations.

In order to see the effect of the mode number m on the amount of power seen at the output, when the m is changed from 1 to 3, that is when *the fourth mode is of interest* in the semiconductor slab guide, the results show an observable, however a very minor change in the output power:

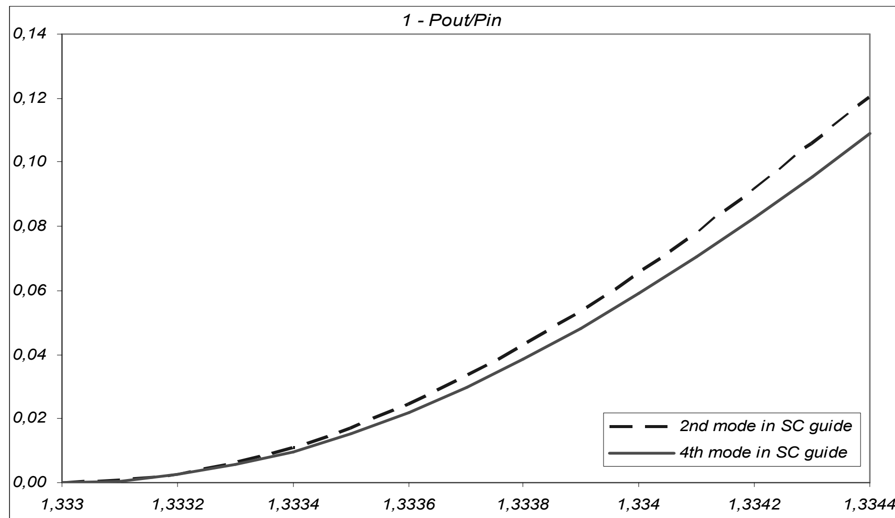

Figure 3-5: Output power vs. n_{out} for configuration #1 when the fourth mode is of interest in the semiconductor slab guide.

In addition, we see that the amount of power coupled to the second waveguide increases in this case, which means that there is less power seen at the output. Comparing with the earlier simulation where the second mode was of interest in the semiconductor guide, we see that for n_{out} values close to 1.3330, both results are similar. However, as the outer refractive index increases, more power is seen at the output for the earlier case. Therefore, since our aim is to sense the changes in the outer layer, we can conclude that using the smaller mode as the mode of interest in the semiconductor slab guide is more advantageous.

Moving onto the wavelength dependence of the critical coupling, we should remember that the expected behavior is a perfect match at a predefined wavelength (in this case at 1.55 µm), and very low matching at the wavelengths away from the critical wavelength. It should be noted that, in all of the wavelength-dependent calculations, the indices of the layers are calculated with respect to each instantaneous wavelength of interest, that is, as a function of the wavelength (i.e. $n_{BCB}(\lambda)$, etc.). The simulations and the calculations present the following wavelength characteristics:

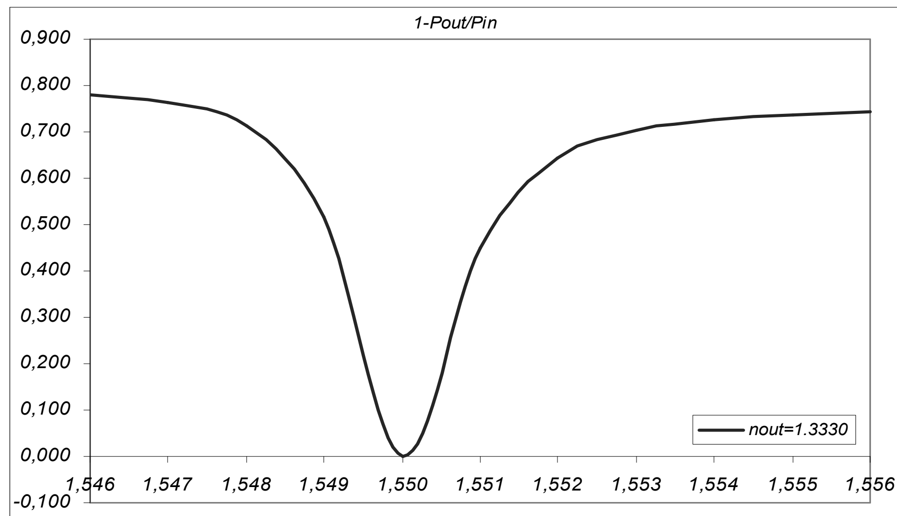

Figure 3-6: Output power vs. wavelength of operation for configuration #1 for n_{out} = 1.3330 and n_{out} =1.3344.

The simulation results show that our expectations are in fact, correct. Moreover, the above figure shows that when the wavelength of operation is shifted by an amount of 1 nm, the output power changes quite a large amount, by an amount of 45 percent. Furthermore, when we observe the sensing characteristics of the device with the multiple wavelength spectrum, we get the following characteristics graph, showing the wavelength spectrum of the device when the outer layer refractive index equals 1.3330 and 1.3344:

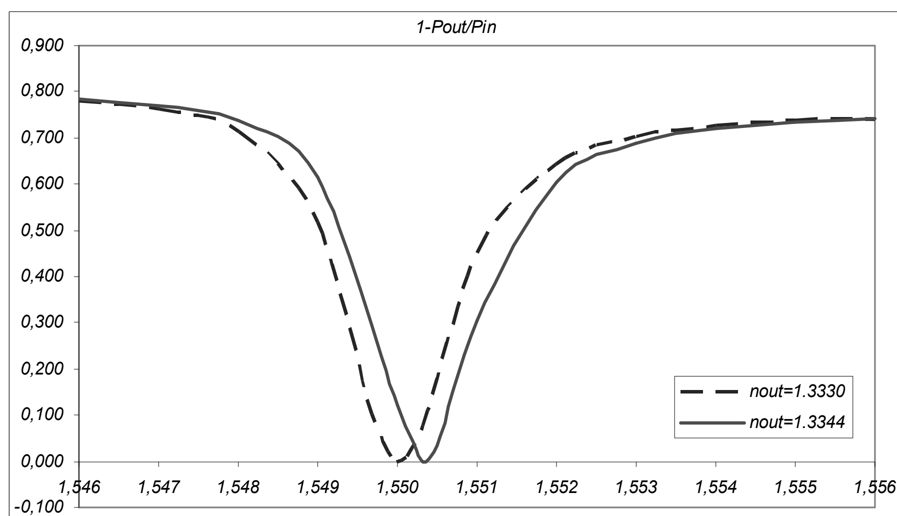

Figure 3-7: Output power vs. wavelength of operation for configuration #1

The above figure shows that the wavelength dependence for the critical coupling prevails for the changing outer layer refractive index. More importantly, the

characteristics show that when the outer layer refractive changes from n_{out} = 1.3330 to n_{out} = 1.3344, there is a *3 Å shift* observed in the wavelength spectrum. Although the amount of spectrum shift is small, this observation should be repeated in the forthcoming designs as well, in order to see the differences, advantages, etc.

3.3.2. Simulation Set #2

The second asymmetric directional coupler sensor configuration is very similar to the first one, as shown in Fig. 3-8:

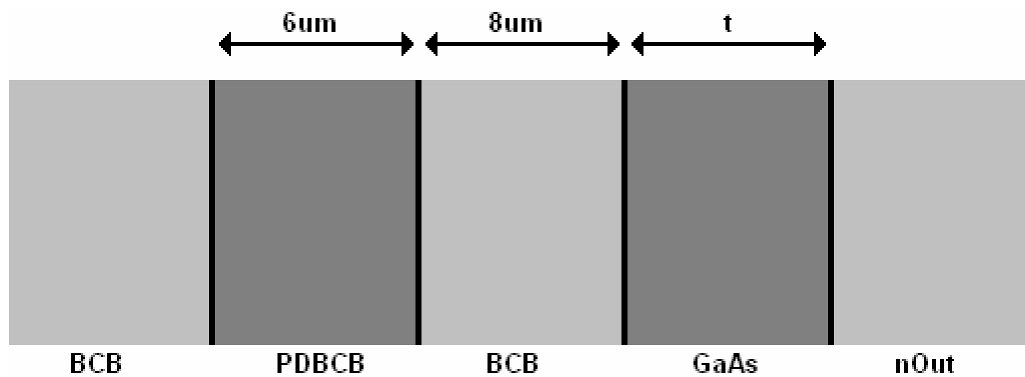

Figure 3-8: Asymmetric directional coupler sensor configuration #2.

The difference between these two configurations that, Configuration #2 is for achieving critical coupling when the outer layer refractive index n_{out} equals 1.5000, the refractive index of crown glass. Other than the outer layer refractive index, the remaining parameters are equivalent to the first configuration. The core polymer layer thickness is 6 μm, the common cladding thickness equals 8 μm, the "base" wavelength of operation is 1.55 μm, and m = 1, meaning that *the second mode is of interest* in the semiconductor slab guide. As in the first simulation set, the primary design parameter is the thickness of the semiconductor core layer, and the method for determining t_{SC} is the same as before. When calculated, the thickness for achieving critical mode matching at 1.55 μm wavelength turns out to be t = 268.392 nm.

Investigating the n_{out} dependence of this configuration, when the output power is calculated with respect to the outer layer refractive index, the following figure is obtained:

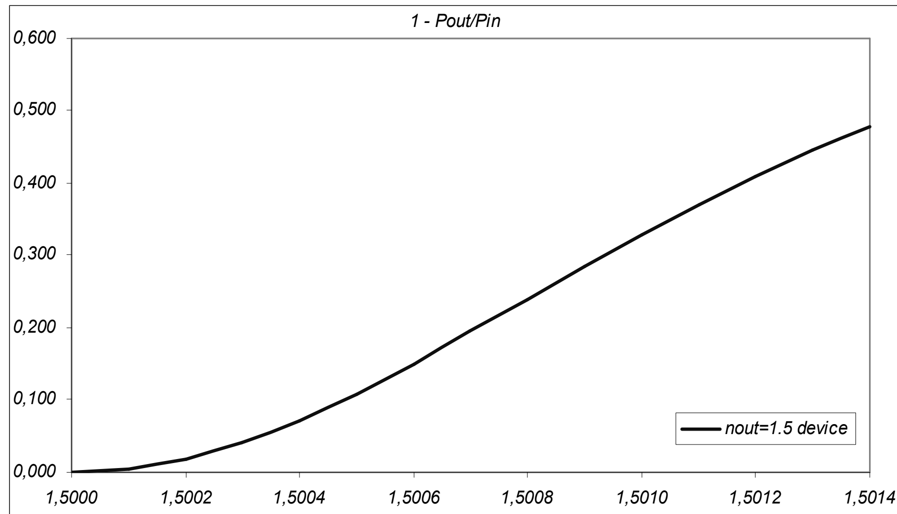

Figure 3-9: Output power vs. n_{out} for configuration #2.

We see from the above graph that, all of the input power is coupled to the second waveguide when the outer layer refractive index equals 1.5000, whereas, as the outer refractive index increases, the amount of power at the output increases, and 50% of the input power is seen at the output when n_{out} equals 1.5014. This ratio was calculated to be 12 % for Simulation Set #1, and this difference between the ratios shows that as the refractive index of the outer layer approaches the refractive index of the common cladding region and also to that of the semiconductor core region, the amount of coupled power increases.

As far as the wavelength dependence of the critical coupling is concerned, the simulations and the calculations present the following wavelength characteristics:

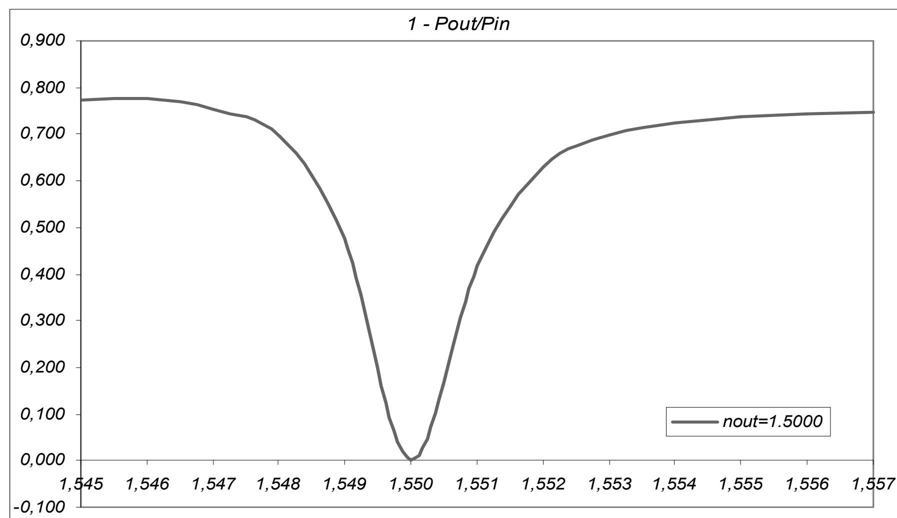

Figure 3-10: Output power vs. wavelength of operation for configuration #2.

The simulation results show similar highly selective characteristics as the previous configuration. Moreover, the above figure shows that when the wavelength of operation is shifted by an amount of 1 nm, the output power changes hugely, by an amount of approximately 40 percent. Furthermore, when we observe the sensing characteristics of the device with the multi-wavelength spectrum, we obtain the following plot, showing the wavelength spectrum of the device when the outer layer refractive index equals 1.5000 and 1.5014:

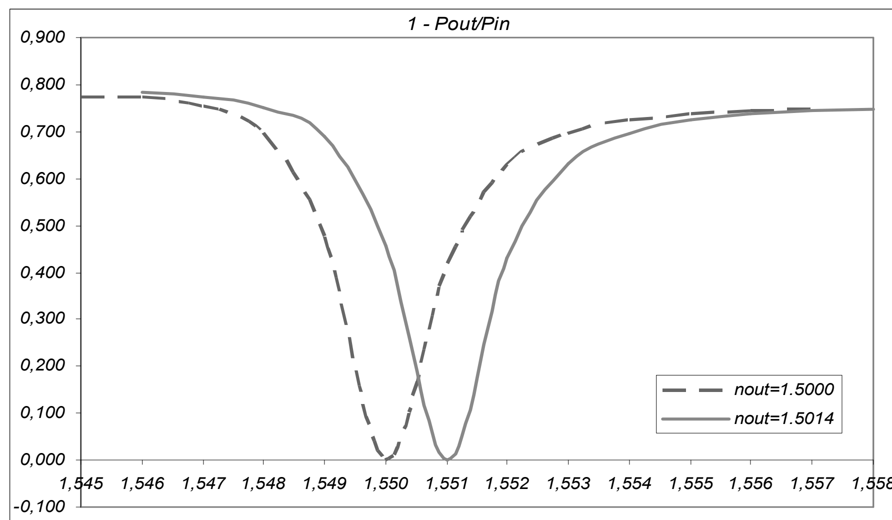

Figure 3-11: Output power vs. wavelength of operation for configuration #2 for n_{out} = 1.5000 and n_{out} = 1.5014.

The above figure shows that the wavelength dependence for the critical coupling prevails for the changing outer layer refractive index. More importantly, the characteristics show that when the outer layer refractive changes from n_{out} = 1.5000 to n_{out} = 1.5014, there is a *10 Å shift* observed in the wavelength spectrum. Compared with the spectrum observed in the previous simulation set, we see that as the outer layer refractive index becomes closer to the refractive index of the common cladding region and also to that of the semiconductor core region, the shift has increased by a factor of more than 3.

3.3.3. Simulation Set #3

The third simulation set employs the same polymer waveguide as the previous sensors; however, it replaces the Gallium Arsenide core layer with a silicon layer in the

semiconductor slab guide, as illustrated in the following figure:

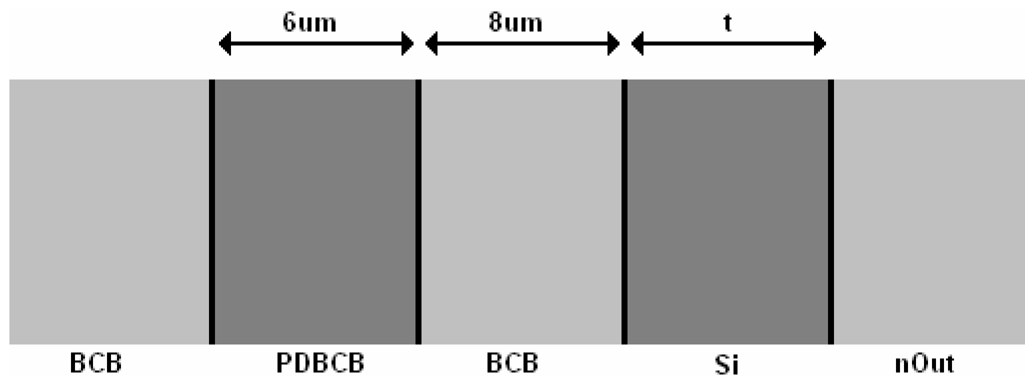

Figure 3-12: Asymmetric directional coupler sensor configuration #3.

The purpose of investigating such a configuration is to observe the device performance when silicon is employed in the structure, which can be considered as a fabrication alternative. The refractive index of silicon being around 3.378 in the spectrum of interest suggests that the device performance and characteristics will be very similar to the devices in which a Gallium Arsenide core layer is employed in the semiconductor slab guide. The thickness t_{SC} to achieve the critical matching condition in the "base" wavelength of 1.55 µm and the outer layer refractive index of 1.3330 is calculated to be t = 279.705 nm; and remaining properties are the same as the first configuration (Simulation Set #1).

Investigating the n_{out} dependence of this configuration, when the output power is calculated with respect to the outer layer refractive index, the following figure is obtained:

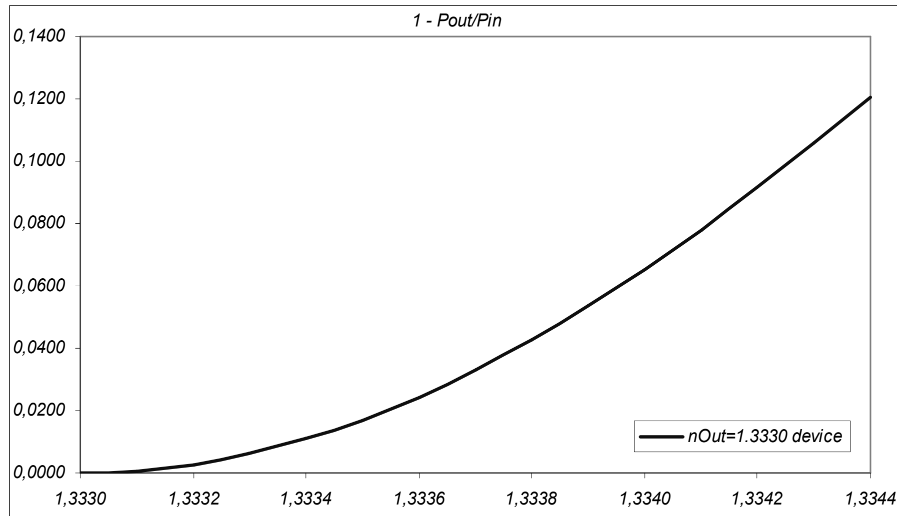

Figure 3-13: Output power vs. n_{out} for configuration #3.

The results obtained with this device are almost identical with Simulation Set #1. All of the input power is coupled to the second waveguide when the outer layer refractive index equals 1.3330, whereas, as the outer refractive index increases, the amount of power at the output increases, and 12% of the input power is seen at the output when n_{out} equals 1.3344.

As far as the wavelength dependence of the critical coupling is concerned, the simulations and the calculations present the following wavelength characteristics:

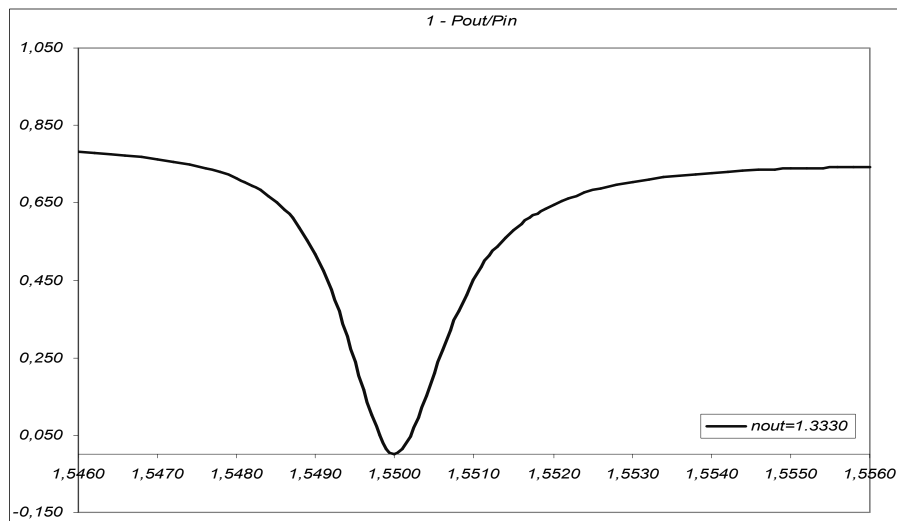

Figure 3-14: Output power vs. wavelength of operation for configuration #3.

As expected, the results show that when the wavelength of operation is shifted by an amount of 1 nm, the output power changes significantly, by an amount of 45 percent,

similar to the equivalent configuration employing gallium arsenide instead of silicon in the core layer. Furthermore, we obtain the following plot, showing the wavelength spectrum of the device when the outer layer refractive index equals 1.3330 and 1.3344:

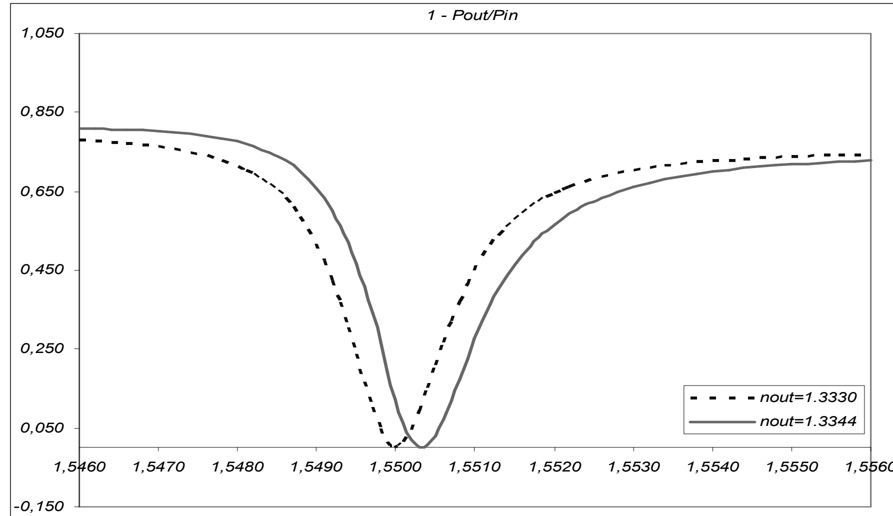

Figure 3-15: Output power vs. wavelength of operation for configuration #3 for n_{out} = 1.3330 and n_{out} = 1.3344.

Once more, the results are as expected. The above figure shows that when the outer layer refractive changes from n_{out} = 1.3330 to n_{out} = 1.3344, there is a *3 Ǻ shift* observed in the wavelength spectrum, similar to Simulation Set #1.

3.3.4. Simulation Set #4

Similar to the purpose of the previous configuration, Simulation Set #5 is the silicon-analog of the Simulation Set #2, as seen in the following figure:

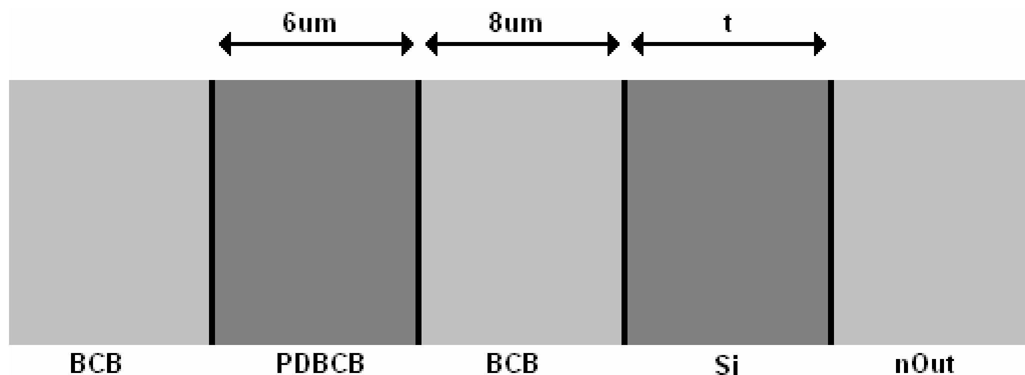

Figure 3-16: Asymmetric directional coupler sensor configuration #4.

This configuration employs an outer layer refractive index of 1.5. The thickness t_{SC} to achieve the critical matching condition in the "base" wavelength of 1.55 μm and n_{out} = 1.5000 is calculated to be t = 268.266 nm; and remaining properties are the same as the second configuration (Simulation set#2).

Investigating the n_{out} dependence of this structure, when the output power is calculated with respect to the outer layer refractive index, the following figure is obtained:

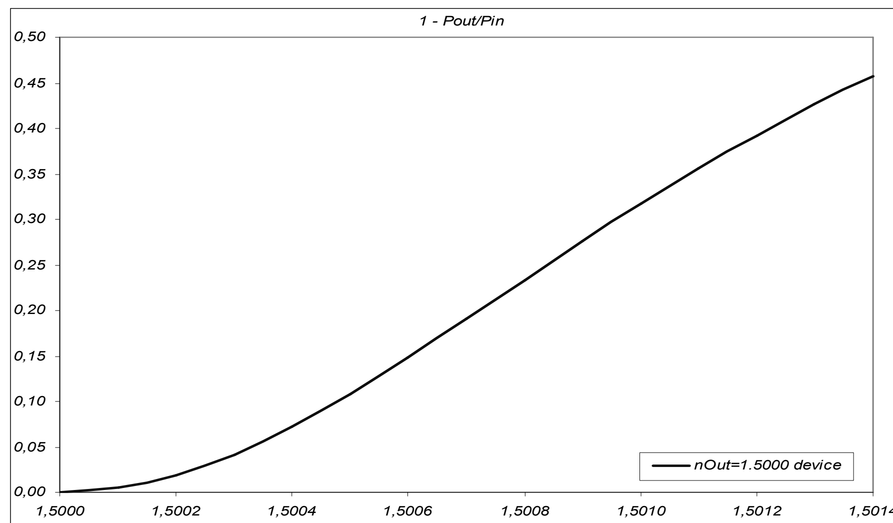

Figure 3-17: Output power vs. n_{out} for configuration #4.

The results obtained show that all of the input power is coupled to the second waveguide when the outer layer refractive index equals 1.5000, whereas, as the outer refractive index increases, the amount of power at the output increases, and 45% of the input power is seen at the output when n_{out} equals 1.5014.

As far as the wavelength dependence of the critical coupling is concerned, the simulations and the calculations present the following wavelength characteristics, where the plot shows the wavelength spectrum of the device for both when the outer layer refractive index equals 1.5000 and 1.5014:

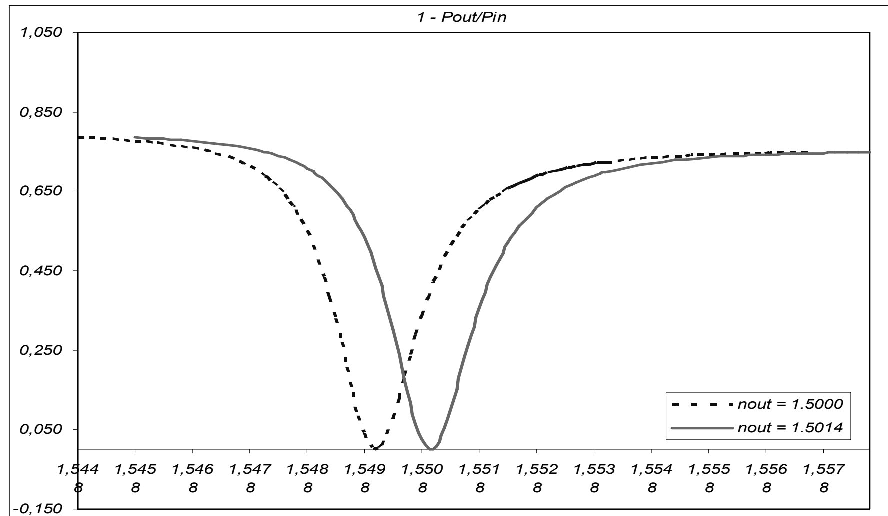

Figure 3-18: Output power vs. wavelength of operation for configuration #4 for n_{out} = 1.5000 and n_{out} =1.5014.

As expected, the results show that when the wavelength of operation is shifted by an amount of 1 nm, the output power changes hugely, by an amount of 42 percent. In addition, we see that when the outer layer refractive changes from n_{out} = 1.5000 to n_{out} = 1.5014, there is a *10 Å shift* observed in the wavelength spectrum, similar to Simulation Set #2.

The last two examples, Configuration #3 and Configuration #4 show that there is no major difference between employing silicon or gallium arsenide layer in the core region of the semiconductor slab guide, and that the device can be realized using any of the two, depending on fabrication issues.

3.3.5. Simulation Set #5

The fifth configuration is based on the initial silicon-employing structure (Simulation Set #3); however, the common cladding region is reduced from 8 μm to 4 μm, and the effects of this change on the device performance and characteristics are to be investigated. The configuration is illustrated in the following figure:

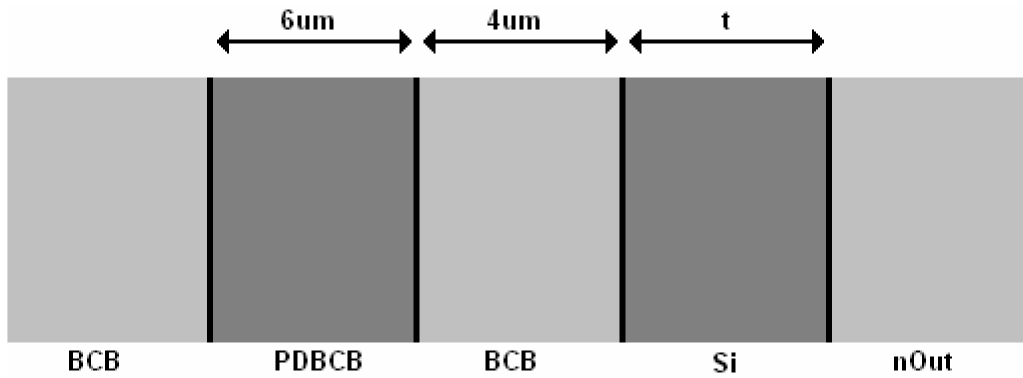

Figure 3-19: Asymmetric directional coupler sensor configuration #5.

The outer layer refractive index n_{out} is taken as 1.3330 and the thickness ensuring the critical match condition is calculated to be t = 279.705 nm. As the previous devices, the mode number is taken to be m = 1, meaning that *the second mode is of interest* in the semiconductor slab guide.

Investigating the n_{out} dependence of this configuration, when the output power is calculated with respect to the outer layer refractive index, the following figure is obtained:

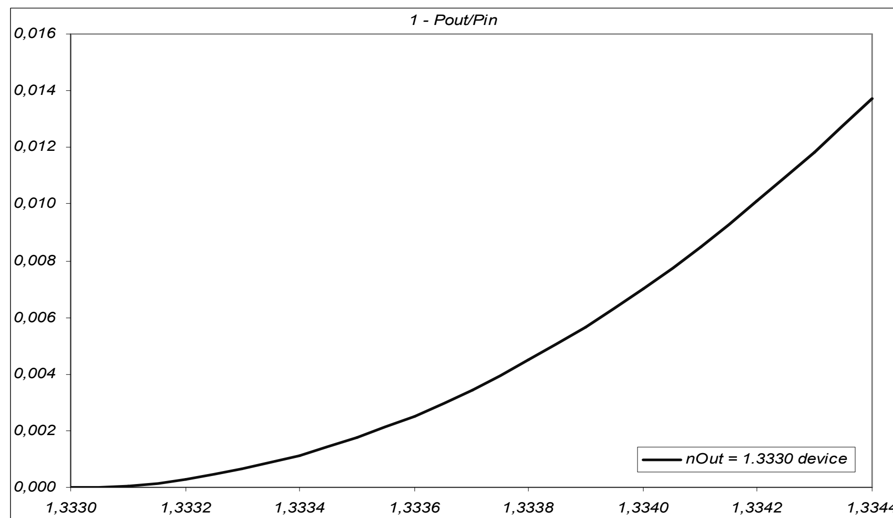

Figure 3-20: Output power vs. n_{out} for configuration #5.

We see from the above graph that, all of the input power is coupled to the second waveguide when the outer layer refractive index equals 1.3330, whereas, as the outer refractive index increases, the amount of power at the output increases an insignificant amount, and 1.4% of the input power is seen at the output when n_{out} equals 1.3344.

As far as the wavelength dependence of the critical coupling is concerned, the

simulations and the calculations present the following wavelength characteristics, where the plot shows the wavelength spectrum of the device for both when the outer layer refractive index equals 1.3330 and 1.3344:

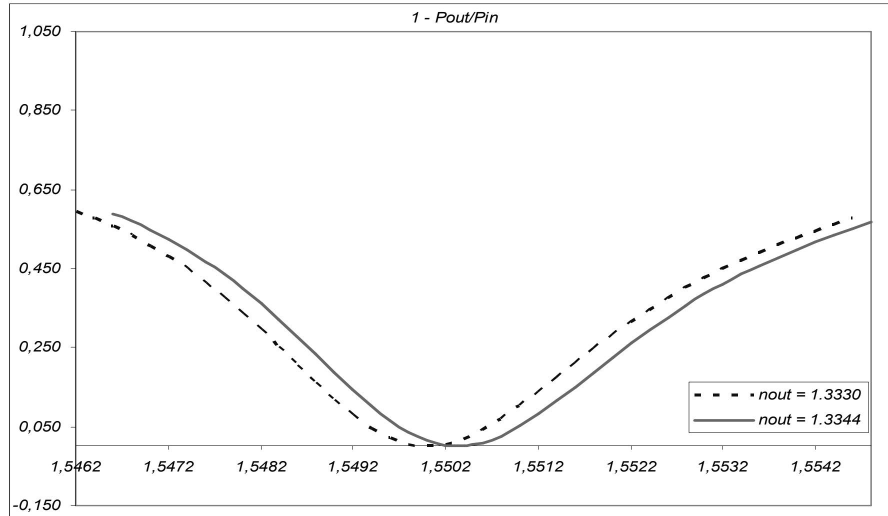

Figure 3-21: Output power vs. wavelength of operation for configuration #5 for n_{out} = 1.3330 and n_{out} = 1.3344.

As with the n_{out} dependence, the multi wavelength characteristics of this configuration are also observed to be rather poor. When the wavelength of operation is shifted by an amount of 1 nm, the output power changes relatively poorly, by an amount of 10 percent. In addition, we see that when the outer layer refractive changes from n_{out} = 1.3330 to n_{out} = 1.3344, there is a *3 Å shift* observed in the wavelength spectrum. The reason for this behavior is that, since the common cladding is thinner in this configuration, the coupling coefficient κ is relatively higher and hence δ/κ is smaller.

3.4. Simulations Summary and Discussion

Having explored the five different configurations, a summary of the general properties of these simulation sets is presented in the following table:

Table 3-1: Summary of the general properties of simulated sensor configurations.

	SC Core	t_{SC} (nm)	T_{clad} (μm)	base n_{out}	$1-P_{out}/P_{in}$ for max n_{out}	Spectral Shift (Å)
Configuration #1	GaAs	279,842	8	1,3330	0,12	3
Configuration #2	GaAs	268,392	8	1,5000	0,50	10
Configuration #3	Si	279,705	8	1,3330	0,12	3
Configuration #4	Si	268,266	8	1,5000	0,45	10
Configuration #5	Si	270,705	4	1,3330	0,014	3

The analysis of these simulations points out some important facts about the device. It can be seen that the device performance is highly sensitive to thickness changes, in the order of nanometers. The dependence of the device performance to the semiconductor layer thickness is briefly investigated in Appendix A.

In addition, a section involving the comparison the performances of the asymmetric directional coupler and the symmetric directional coupler structures is presented in Appendix B, where the results presented show the advantage of the asymmetric directional coupler over the symmetric structure.

An analysis of relative performances is in order. First of all, for the purpose monitoring refractive index changes around the base index of n = 1.3330, configurations #1 and #3 clearly rule out configuration #5. These two simulation sets demonstrate a variation of 12 % at the output power for the fixed wavelength of 1.55 μm, or alternatively a spectral shift of 3 Å for a multi wavelength spectral analysis.

Furthermore, for the purpose of monitoring refractive index changes around the base index of n = 1.5000, both of the configurations #2 and #4 exhibit an equivalent performance, demonstrating a variation of around 50 % at the output power for the fixed wavelength of 1.55 μm, or alternatively a spectral shift of 10 Å for a multiple wavelength analysis.

Here, one point to note is that, sensor configurations #1 and #2 employ gallium

arsenide cores in their semiconductor slab guides, whereas their equally performing counterpart configuration #4 employs silicon. Due to the very near refractive indices of the gallium arsenide and silicon, the choice of using one of these materials in place of the other becomes trivial in terms of the device performance. Then, the preference of materials becomes an issue of the fabrication.

Considering the microelectronic fabrication facilities and capabilities present at Sabancı University, employing silicon in the device structures turns out to be the clear choice. Hence, the sensor configurations labeled #3 and #4 become the main goal of fabrication, testing and characterization procedures.

3.4.1. A Blood Glucose Sensor

The sensor structure presented in this work can be utilized in many different purposes, and a particular application is the sensing of the glucose concentration in human blood.

Related work on the purpose of sensor configuration #3 has been carried out by Liu, et. al [32], where they reported a refractive index change of 0.0014 when the sugar (glucose) concentration was increased by 1 percent. Considering that the normal glucose concentration of human blood being in the range of 0.07g/100mL – 0.16g/100mL and the refractive index of human blood being $n \approx 1.3334$ in this range, together with the output ratio of sensor configuration #3 being 0.011 for $n = 1.3334$; we can normalize the output of sensor configuration #3 with respect to this value as shown in the figure below, where the marked spot on the plot depicts the reference point for power normalization:

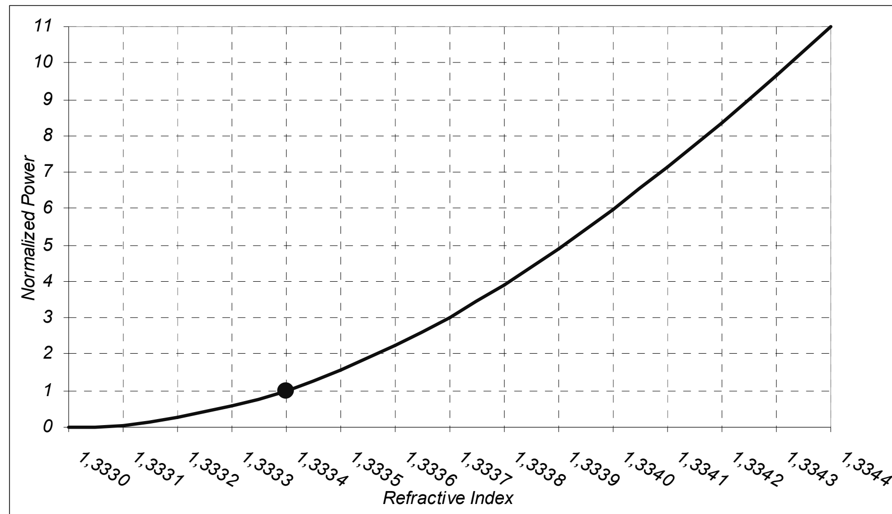

Figure 3-22: Normalized output of configuration #3 with respect to normal human blood refractive index.

Moreover, performing the same normalization with respect to the normal glucose level in human blood, we obtain the following plot, where the marked spot on the plot depicts the reference point for power normalization:

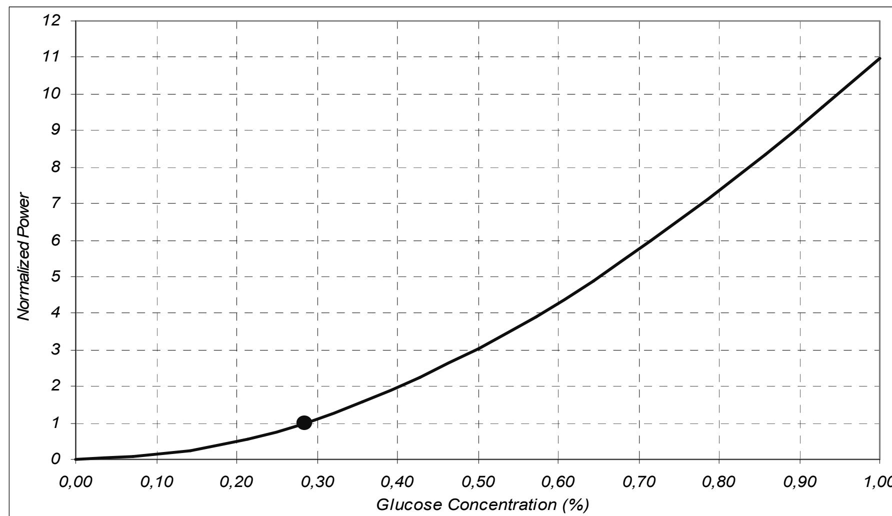

Figure 3-23: Normalized output of configuration #3 with respect to normal human blood glucose level.

The plots show that a 0.007% change in the glucose level is sensed per 0.0001 refractive index change, which corresponds to a concentration of approximately 7mg/100mL. In addition, it can be seen that a 0.1% change in the glucose level changes the output almost 100%. In their comparable design, Liu, et al. has reported an approximately 5% change in the output for the same range of 0.1% change in the

glucose level [32].

In a more recent report, Borges, et al. presented a 17% change in the output for the range of glucose level between 0% and 1% [33], whereas Liu, et al. had reported a 30% change [32]. Here, we present an approximately 10 *times* change in the output for the same range.

CHAPTER 4

DEVICE FABRICATION

4.1. Introduction

The realization of the devices employs conventional semiconductor fabrication methods. Using readily available fabrication techniques such as thin-film coating, spin coating and etching, the devices can be fabricated along the process steps of any silicon or silicon-on-insulator based device and hence integration can be achieved without introducing any additional cost.

4.2. Materials and Processes

In order to realize the final structure of the waveguide, several different process steps must be performed using different materials for the structure, namely, BCB, PDBCB, and silicon layers.

4.2.1. Fabrication of BCB Layers

BCB (Benzocyclobutene) is a thermally produced polymer generally used as a dielectric layer in microelectronic fabrication, and DOW Chemical Company supplies various types of BCB products under the product label Cyclotene 3022 series, as well its characteristics and electrical, mechanical and optical properties [34]. BCB has been used in the microelectronics industry as an interlayer dielectric material [35-37], providing the functions of surface smoothing and surface passivation. Besides its electronic use, it has also been used in the field of optoelectronics as both the core and the cladding material of various waveguide structures, which are used as optical interconnects, optical modulators, optical filters, etc. [27, 38-42].

Fabrication of the BCB layer employs an initial spin-coat of the uncured polymer on the substrate surface, where the final thickness of the coated polymer depends on the spin speed [34]. DOW Chemical Company supplies several Cyclotene 3022 types with different viscosities that produce different final thicknesses depending on the spin speed. The BCB type with product label Cyclotene 3022-57, to be used in fabrication, leads to a cured thickness range between 5 μm and 17 μm depending on the spin speed [34]. DOW Chemical reports for Cyclotene 3022-57 an after-cure thickness of 5.55 μm @ 5000 rpm, 6.20 μm @ 4000 rpm, 7.21 μm @ 3000 rpm, 9.04 μm @ 2000 rpm, and 13.8 μm @ 1000 rpm spin speed.

Spin-coated BCB must be cured to attain its final material properties. The curing process must be performed in an inert atmosphere (preferably in a nitrogen or argon purged tube furnace) due to the oxidation susceptibility of BCB at temperatures above 100 ºC [34]. The curing process of Cyclotene 3022 products involves two different methods, namely, the partial (soft) cure and full (hard) cure.

The partial cure of BCB is used when successive coats or multilayer structures are employed, where multiple levels of BCB are in contact in the structure. DOW Chemical recommends a 40 min partial cure at a temperature of 210 ºC, where approximately 80% of the material polymerizes at the end of the process. The full cure is used as the final cure of BCB when all of the polymer layers in the structure are established. DOW Chemical suggests a 60 min full cure at a temperature of 250 ºC, where approximately 100% of the material polymerizes at the end of the process. Fig. 4-1 illustrates the ratio of the polymerized BCB with respect to curing duration and temperature [34].

A partial cure profile recommended by DOW Chemical is a 15-minute ramp to 150 ºC, a 15-minute soak at 150 ºC, followed by a ramp to 210 ºC, with a 40-minute soak at 210 ºC, and finally a natural cool-down to around 150 ºC [43].

The recommended profile for the full cure is a 15-minute ramp to 150 ºC, a 15-minute soak at 210 ºC, followed by a ramp to 250 ºC, with a 60-minute soak at 250 ºC, and finally a natural cool-down to around 150 ºC [43]. A point to note here is that, despite the safety margin of 150 ºC for the oxygen susceptibility of the polymer, experience has shown that it is not advisable to remove the sample from the furnace at temperatures above around 70 ºC – 80 ºC. Therefore, the natural cool-down stages should be performed down to the temperatures around 75 ºC.

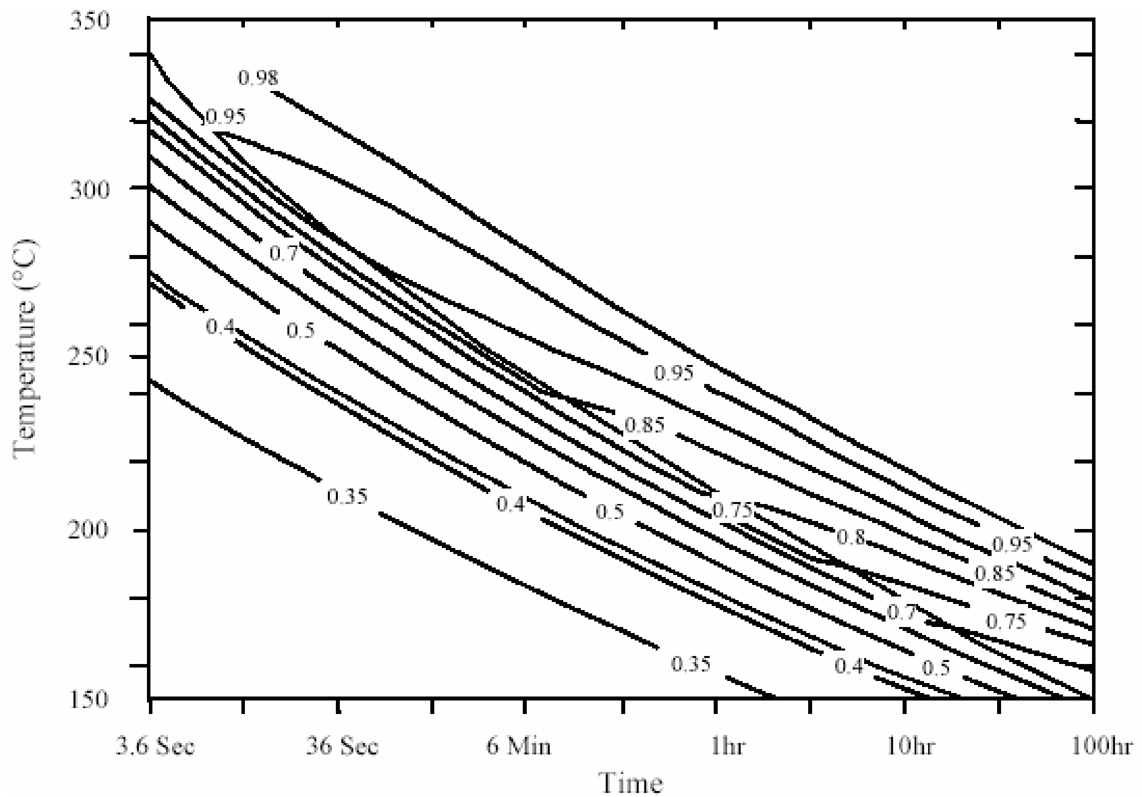

Figure 4-1: Ratio of the polymerized BCB with respect to curing duration and temperature for the full cure process.

4.2.2. Fabrication of PDBCB Layer

PDBCB (Photodefinable Benzocyclobutene) is a photosensitive type of BCB. Supplied by DOW Chemical Company under the product label Cyclotene 4000 series, PDBCB basically has the same characteristics and electrical, mechanical and optical properties as BCB [43]. Similar to BCB, PDBCB has also been used in the microelectronic industry [2], providing the functions of surface smoothing and surface passivation. Furthermore, it has also been used in the field of optoelectronics as the core material of various waveguide structures that are used as optical modulators, optical filters, etc [27, 42].

Fabrication of the PDBCB layer is similar to that of the BCB layer, with additional exposure and develop processes. PDBCB process employs an initial spin-coat of the uncured polymer on the substrate surface, where the final thickness of the coated polymer depends on the spin speed [43]. DOW Chemical Company supplies several Cyclotene 4000 types with different viscosities that produce different final thicknesses depending on the spin speed. The PDBCB types with product labels Cyclotene 4024-40 and Cyclotene 4026-46, to be used in fabrication, lead to a thickness range between 3 μm and 8 μm, and between 7 μm and 15 μm, respectively. DOW Chemical reports for

Cyclotene 4024-40 an after-cure thickness of 3.7 µm @ 5000 rpm, 4.1 µm @ 4000 rpm, 4.8 µm @ 3000 rpm, 5.9 µm @ 2000 rpm, and 7.2 µm @ 1500 rpm spin speed. Moreover, DOW Chemical reports for Cyclotene 4026-46 an after-cure thickness of 7.3 µm @ 5000 rpm, 8.1 µm @ 4000 rpm, 9.4 µm @ 3000 rpm, 11.6 µm @ 2000 rpm, and 14.2 µm @ 1500 rpm spin speed.

Spin-coated PDBCB is then soft baked in order to evaporate the residual solvent and decrease the tackiness of the material for hard contact lithography, where the soft bake duration and temperature depend on the substrate composition and also on the film thickness [43]. DOW Chemical recommends hot plate soft bake temperatures depending on the pre-bake PDBCB thicknesses. Table 4.2-1 depicts these recommended soft bake temperatures for a given bake time of 90 seconds [43].

Table 4-1: Recommended soft bake temperatures with respect to pre-bake PDBCB thicknesses, for a given soft bake time of 90 seconds.

PDBCB pre-bake thickness	Hot plate soft bake temperature
< 4.5 µm	60 ºC
4.6 µm – 6.6 µm	65 ºC
6.7 µm – 8.7 µm	70 ºC
8.8 µm – 10 µm	75 ºC
10.1 µm – 11.4 µm	80 ºC
11.5 µm – 15.6 µm	85 ºC
> 15.6 µm	90 ºC

On the other hand, studies have shown that the parameters for the soft bake are highly pattern dependent [44]. For devices involving waveguide patterns, it has been shown that ideal soft bake temperature for Cyclotene 4024-40 must be between 70 ºC and 90 ºC; and that ideal soft bake temperature for Cyclotene 4026-46 must be between 75 ºC and 100 ºC. It has been experimentally shown that for a soft bake duration of 90 seconds, a temperature of 80 ºC for Cyclotene 4024-40 and a temperature of 90 ºC for Cyclotene 4026-46 leads to the desired results [44].

Following the soft bake, exposure is the next step. DOW Chemical reports that a contact aligner with power level adjusted for a level of radiation at 365 nm, can be used for the task, and that exposure dose should be adjusted according to the pre-exposure film thickness. Consequently, the exposure dose for Cyclotene 4024-40 should be 20

mJ/cm^2 per µm film thickness, and the exposure dose for Cyclotene 4026-46 should be 60 mJ/cm^2 per µm film thickness [43]. It should be noted that the polymer films should cool down to room temperature before the exposure; and also that Cyclotene 4000 series resins act like negative photoresists, that is, exposed regions remain on the structure following the development stage [43].

The next step is the development of the films, and DOW Chemical supplies the developer with product label DS2100 for this process. Puddle development is recommended for this particular developer instead of an immersion development [45]. The puddle development method is as follows: First, a puddle of developer DS2100 is dispensed on the sample rotating at a slow speed, helping the developer spread on the surface. Then, the developer is allowed to remain on the sample to let the unexposed areas dissolve for a certain duration. The end-point of the development process can be determined visually, with the observation of color fringes on the developed portions of the sample [45]. At the end of the puddle time, the sample is rinsed by a 10 second spray of DS2100 developer while spinning at 500 rpm. It should be noted that the developer and the rinse solutions are the same, namely DS2100. After the rinse process, the sample should be spin-dried at a speed of around 5000 rpm for 30 seconds to remove the developer and to dry the sample [43].

The development process is completed with a post-develop bake process typically for 60 seconds at a temperature in the range of 60 ºC – 90 ºC to ensure the dryness of the films and to stabilize the side-walls [43].

Following the development process, the next step is the cure process, where the cure conditions and the parameters for the partial and full cures for PDBCB are exactly the same as for BCB, described in the previous subsection on Fabrication of BCB Layers.

4.2.3. Fabrication of Semiconductor Layer

The semiconductor or namely the silicon core region in the device is fabricated by thin-film deposition by the means of sputtering. According to our fabrication experience, obtaining the desired sputtered silicon layers is possible. The fabrication process employs 200 W of DC power with an argon flow rate of 35 sccm in to the chamber, together with a the base pressure of 0.25 mbar, and a chamber temperature of 250 ºC. With these process parameters, the final thickness of the sputtered silicon layer was measured to be 360 nm for a duration of 20 minutes, and 660 nm for a duration of 40

minutes. These figures correspond to a deposition rate of approximately 17 nm/min. Then, using the above recipe, a process duration of 16.4 minutes should be employed for Device #4, and a duration of 15.8 minutes should be employed for Device #5.

4.2.4. Fabrication of Ridge Structure – Reactive Ion Etching of BCB

The ridge structure in the device is fabricated by dry-etching, that is reactive ion etching to be exact. Since the ridge structure is on the BCB region, a BCB Plasma etch should be performed in order to form the device structure. Reactive ion etching of BCB is performed using a mixture of oxygen and a fluorine gases, where both the etch rate and the smoothness of the etched are controlled by the ratio of the fluorine gas in the oxygen-based mixture [46]. The reason for this effect of the fluorine gas is the presence of silicon in the backbone of BCB polymer [34].

Masking in the reactive ion etching of BCB is an important issue, where both hard masks and soft masks can be used for the process. Hard masking commonly employs the deposition of metal or silicon oxide or silicon nitride on the surface, followed by patterning by the means of photolithography, and etching. Once the reactive ion etching is completed, the mask has to be removed from the surface without damaging the underlying polymer. Since fluorine is present in the gas mixture[46], the range of hard mask materials that can be consistently used are limited. Even if the selectivity concerning the hard mask is not an issue, using a hard mask increases the process complexity [47].

Using a soft mask (i.e., a photoresist mask) reduces the process complexity of the etch process by eliminating the deposition, patterning and stripping processes. The disadvantage is the reduced etch selectivity, however the effect of this disadvantage can be overcome mostly by choosing appropriate parameters for the etch process [47].

Our experimental results have shown that, desirable etch results are obtained when a total flow rate of 45 sccm with an O_2 rate of 11%, employing 300 W of RIE RF power. The background pressure and the chamber pressure values for the mentioned parameter set are 180 µbar and 260 µbar, respectively.

4.3. Overall Process Flow

Having discussed the fabrication techniques for each layer employed in the device structure individually, we can now present the overall process flows and fabrication

recipes for both devices. Note that, the fabrication steps of both devices are identical, except for the deposition durations of their silicon layer, due to the difference in the thicknesses of the two regions.

The fabrication of the device starts with the spin-coating of uncured BCB on the substrate. The thickness of this layer should be as thick as possible, since this layer will be the lowest cladding region of the sensor structure, and it is critical to isolate the core region of the polymer guide from the substrate, or any other structure sitting under the sensor structure. And so, using the BCB product with name designation Cyclotene 3022-57 and spin-coating with a spin speed of 1000 rpm result in a final thickness of 13.8 μm, which suffices the isolation needs of the device.

Once the BCB is spin-coated, the next step is the partial cure of the BCB. A full cure is not employed at this point, because subsequent BCB and PDBCB layers will also have to be full cured following their spin-coat, and two-time full cure of a BCB region must be avoided, as discussed in the previous sections. The partial cure of the first BCB region involves a 15-minute ramp to 150 ºC, a 15-minute soak at 150 ºC, followed by a ramp to 210 ºC, with a 40-minute soak at 210 ºC, and finally a natural cool-down to around 75 ºC; in a nitrogen-purged furnace.

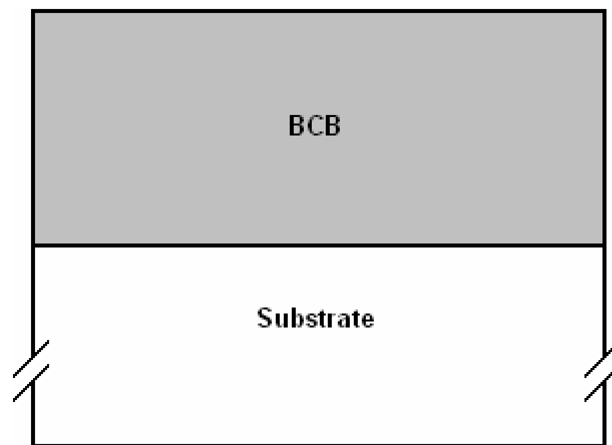

Figure 4-2: Fabrication step #1 – spin-coat and partial cure of BCB.

Once the spin-coat and the partial cure of the BCB layer is performed, the next step in the fabrication is the dry etching of the BCB layer which will later form the ridge structure in the finished polymer waveguide. The dry etching of the BCB layer employs reactive ion etching, and the process parameters of a total flow rate of 45 sccm with an O_2 rate of 11%, employing 300 W of RIE RF power, where the background pressure and the chamber pressure values are 180 μbar and 260 μbar respectively, produces the

necessary ridge structure in the waveguide.

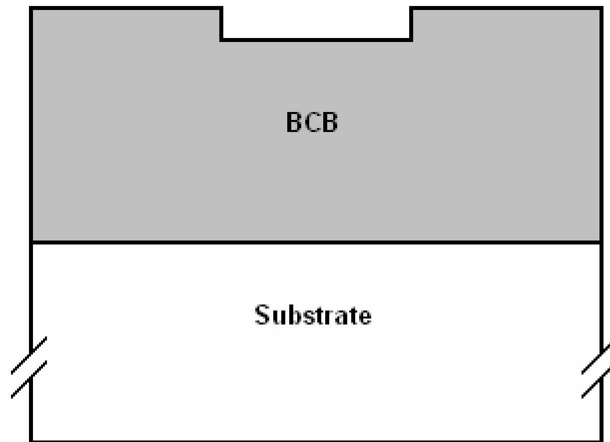

Figure 4-3: Fabrication step #2 – reactive ion etching of BCB.

The next fabrication step is the spin-coating of PDBCB on to the initial BCB layer, to form the core region of the polymer waveguide. Remembering that the thickness of the core layer is set to be 6 μm, and in the light of the discussions in the previous sections, we conclude using the BCB product with name designation Cyclotene 4024-40, and a spin speed of 1940 rpm leads to the desired PDBCB thickness.

Then, the next step is the soft-bake of the PDBCB, which is a 90 second bake on the hot-plate at a temperature of 65 ºC. Once the structure cools down to the room temperature, the PDBCB layer is then exposed using a contact aligner with power level adjusted for a level of radiation at 365 nm. The exposure dose for the PDBCB layers in the devices is 120 mJ/cm^2.

Following the exposure of the PDBCB layer, the PDBCB layer is then puddle developed with DS2100 developer, precisely as described in the previous sections. After the develop process, the structure is soft baked on a hot plate for 60 seconds at a temperature of 90 ºC. The fabrication of the PDBCB layer ends with the partial cure of the polymer. The partial cure conditions and parameters are exactly the same with the partial cure scheme of the BCB layer.

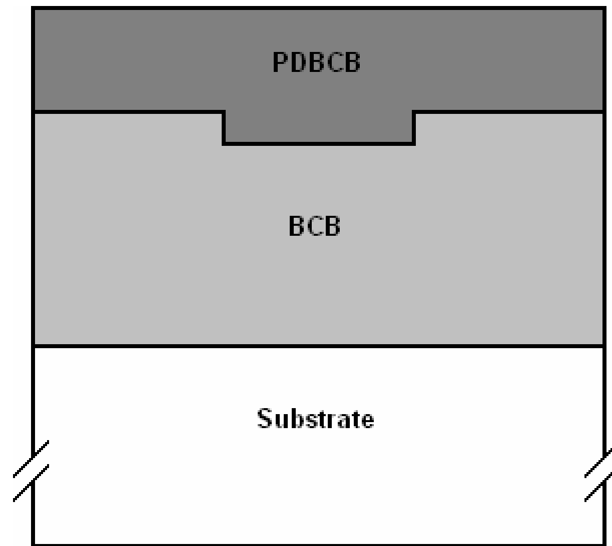

Figure 4-4: Fabrication step #3 – spin-coat, exposure, developing.

Once the PDBCB layer is set (though both BCB and PDBCB layers has not been full-cured yet), the next step is the fabrication of the common cladding layer. This involves the spin-coating and partial cure of a second BCB layer.

Remembering that the thickness of the common cladding region is 8 μm, and in the light of the discussions in the previous sections, we selected the BCB product with name designation Cyclotene 3022-57, for which a spin speed of 2460 rpm provides the desired BCB thickness.

Following the spin-coat, the next step is the full cure of the BCB layer, which is also, the full cure of the underlying PDBCB and BCB layers.

The full cure process involves a 15-minute ramp to 150 ºC, a 15-minute soak at 150 ºC, followed by a ramp to 250 ºC, with a 60-minute soak at 250 ºC, and finally a natural cool-down to around 75 ºC; in a nitrogen-purged tube furnace.

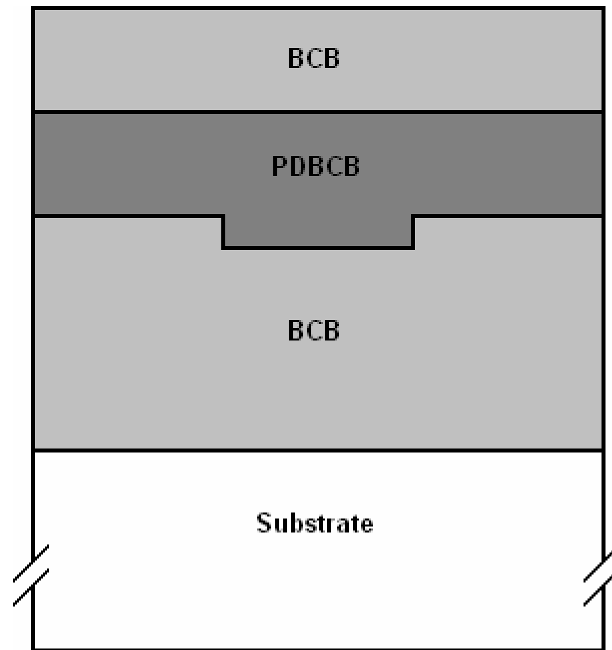

Figure 4-5: Fabrication step #4 – spin-coat of BCB and full cure.

Once the fabrication of the polymer films are completed, the final step of fabrication of the whole device is the fabrication of the semiconductor layer, which involves the thin film deposition of silicon via sputtering. The sputtering process employs 200 W of DC power with an argon flow rate of 35 sccm in to the chamber, together with a base pressure of 0.25 mbar, and a chamber temperature of 250 ºC. For Device #4, in order to achieve a final thickness of 279 nm, the deposition duration is 16.4 minutes; where as for Device #5, the deposition duration is 15.8 minutes in order to achieve a final thickness of 268 nm.

The deposition of the silicon layer completes the device fabrication. The complete device structure is achieved by the coming together of the fabricated device with the medium to be monitored. The final structure at the end of the fabrication can be seen below, in Fig. 4-6:

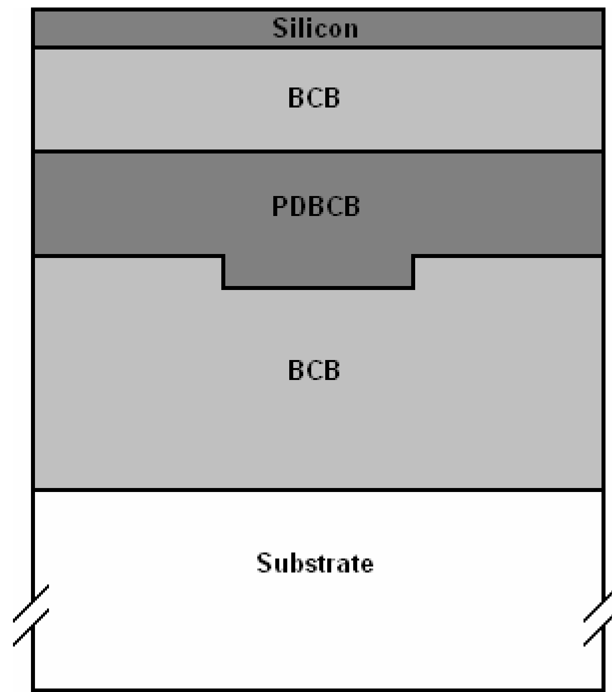

Figure 4-6: Final step of fabrication – thin-film deposition of the silicon layer.

CHAPTER 5

CONCLUSIONS AND FUTURE WORK

5.1. Conclusions

In this work, a new optical chemical sensor was designed. The structure is based on a highly asymmetric directional coupler, where the asymmetry implies a high index difference between the core layers of the waveguides in the coupler, rather than an asymmetry in the geometry. The device structure is generic, and can be modified, and also can be improved for specific applications.

The designed device presents a very high sensitivity on both the operating wavelength, and the index of refraction of the target material. Therefore, the monitoring can be performed in two alternative ways, namely, by monitoring the output power at a specified wavelength of operation, or by monitoring the whole multi-wavelength spectrum for a changing refractive index. Both of these techniques were demonstrated in the device simulations, and the results certified the expectations. Besides, simulations were also supportive in moving towards an optimum design for specific applications.

For the particular application of sensing of the glucose concentration in human blood, when the glucose level was changed in the range between 0% and 1% the device has presented an approximately 10 times change in the level of output power, whereas previously reported devices presented changes around 0.3 times in the output power level.

The sensor employs contemporary microelectronic fabrication techniques and can easily be integrated with various microelectronic components. The complete top-down fabrication scheme for the devices was presented, giving specific recipes and techniques. The materials to be used in the fabrication were selected to yield the best results in terms of device performance. In addition, fabrication processes for each individual layer

were optimized in order to obtain the desired device structure.

5.2. Future Work

As the future work of this research, the initial aim is the fabrication of the devices. Following the fabrication are the testing and characterization of the sensors. According to the results of the characterization, further optimizations in the design may be performed.

Moreover, employing different semiconductor materials in the coupler structure is also a work to be done. For this task, initial candidate for the semiconductor material in the device is ZnO (zinc oxide), which has a refractive index around 2.1 in the operating wavelength of 1.55 μm. The effects of using ZnO on the device performance, and a comparison between the three semiconductors to be in the device (GaAs, Si and ZnO) are to be studied. Employing dielectrics like SiO_2 (silicon dioxide) and studying the effects are also options for the work to be done in the future.

Furthermore, modifying the generic device structure for the sensing of different materials is another preference in the future goals.

In addition, integration of the device with various other IC or semiconductor components is planned. Integrating the structure with its own readout circuitry, for example, on the same chip is one of the ultimate goals of this research.

APPENDIX A

BRIEF INVESTIGATION OF THICKNESS DEPENDENCE OF THE WAVELENGTH OF OPERATION

A.1. Introduction

The aim of this section is to briefly investigate the sensitivity of the device structure to the thickness of the semiconductor core region. The analysis involves the observation of the changes in the center wavelength with changing semiconductor layer thickness.

A.2. Simulation Method and Results

For this task, asymmetric directional coupler sensor Configuration #4 was taken as the reference. The device structure is illustrated in Fig. A-1:

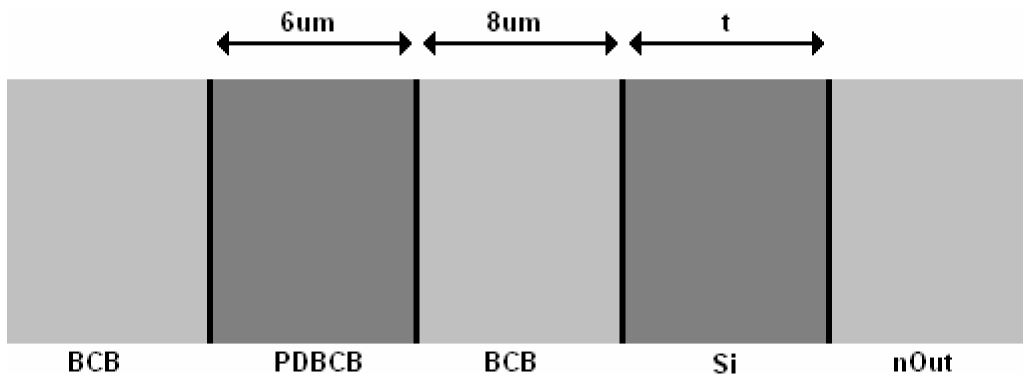

Figure A-1: Device structure for thickness-dependence analysis

In order to achieve comparable results, the initial thickness of the semiconductor layer in the slab waveguide has been set the same as its original value, achieving critical

mode-matching at the operating wavelength of 1.55 μm, when the outer layer refractive index equals n_{out} = 1.5000. Then, in order to observe the affect of the changing *t*, the thickness was changed by small amounts and the wavelengths of critical-mode matching corresponding to each value of *t* were recorded. As a result of this analysis, the following plot was obtained:

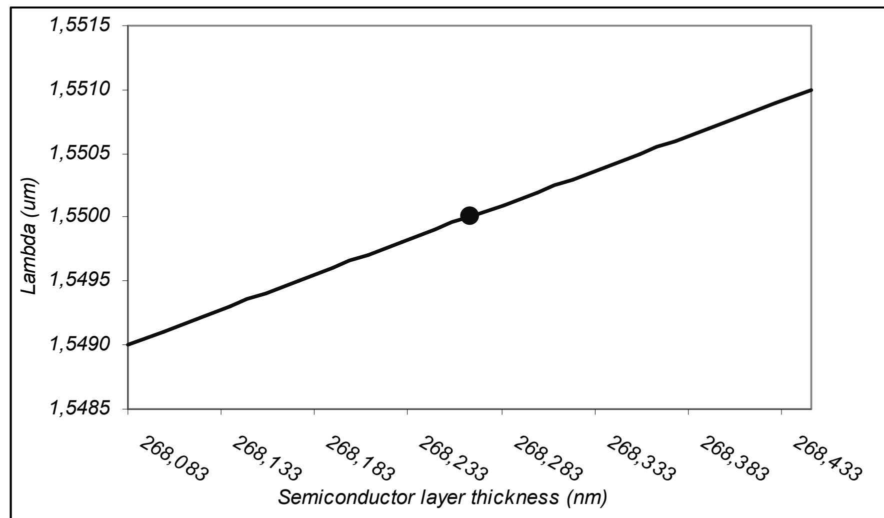

Figure A-2: Wavelength of mode-matching vs. semiconductor layer thickness

In the figure above, the marked spot depicts the thickness which the sensor Configuration #4 employs for obtaining mode-matching at the operating wavelength of 1.55 μm. The rest of the plot shows the deviation in the operating wavelength when the thickness varies from its original value. It can be seen that the wavelength of critical mode-matching is highly dependent on *t*, and this dependence is in the order of sub-nanometers. This dependence is a crucial fact in terms of the fabrication techniques and shows the level of precision that should be employed in the fabrication of the semiconductor layer in order to obtain critical mode-matching at a specific wavelength. However, we should note that a change in the wavelength where the phase matching occurs will not affect the overall characteristics of the sensor.

APPENDIX B

BRIEF ANALYSIS OF THE SYMMETRIC DIRECTIONAL COUPLER

B.1. Introduction

The aim of this section is to compare the performances of the asymmetric directional coupler and the symmetric directional coupler structures. The analysis involves the n_{out} dependence of the symmetric structure, as well as its multiple-wavelength spectrum characteristics.

B.2. Simulation Method

The simulation method employed in the simulation of the symmetric structure is the same as the one employed for the asymmetric structure. The same simulation algorithms have been used in the analysis as the simulation sets presented in Chapter 3 on Simulations and Results.

B.3. Simulations and Results

The device structure is a symmetric directional coupler, where unlike the asymmetric structures investigated in the whole of this work, the cores of the two waveguides in the coupler structure are identical. To be exact, both waveguide cores consist of PDBCB polymer regions. The outer (environmental) region in the structure is kept as the n_{out} layer as in the previous simulations in order to be able to make a better comparison between the two structures.

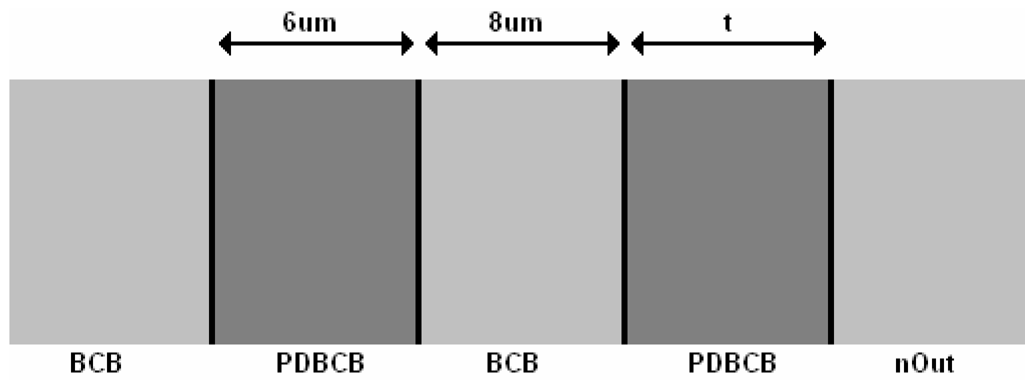

Figure B-1: Symmetric directional coupler sensor configuration.

As seen in the figure, the thickness of the lower PDBCB layer is set as 6 µm, that of the common cladding is set as 8 µm, and also, the refractive index of the outer layer is set to be n_{out} = 1.5000. With these figures, this configuration can be considered as the "symmetric" analog of Configuration # 4, which as the same lower core and common cladding lengths and the same initial outer layer refractive index. However, the upper waveguide is designed to be single-mode, in order to guarantee critical matching.

When calculated, the thickness for achieving critical mode matching at the operating wavelength of 1.55 µm turns out to be t = 8.172 µm. Investigating the n_{out} dependence of this configuration, when the output power is calculated with respect to the outer layer refractive index, the following figure is obtained:

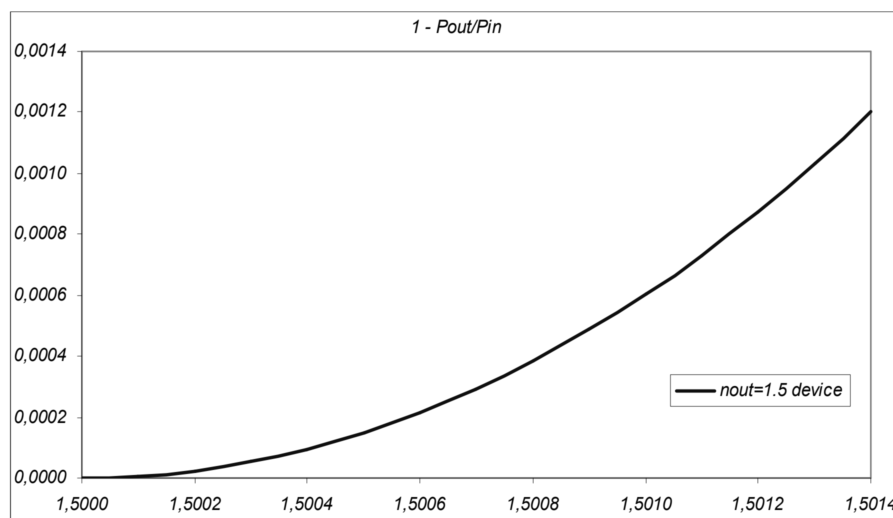

Figure B-2: Output power vs. n_{out} for the symmetric device.

As seen in the figure, the device characteristics exhibit a similar form of plot as the asymmetric structures. On the other hand, whereas all of the input power is coupled

to the second waveguide when the outer layer refractive index equals 1.5000, as the outer refractive index increases, the amount of power at the output increases a very insignificant amount, and only 0.001% of the input power is seen at the output when n_{out} equals 1.5014. Moreover, if we compare the power-levels for the both structures, it can be seen that the magnitude of power seen at the output of the symmetric device is totally ignorable compared to that of the asymmetric device; and this is illustrated in the plot below, where the outputs of the symmetric configuration and configuration are shown on the same plot:

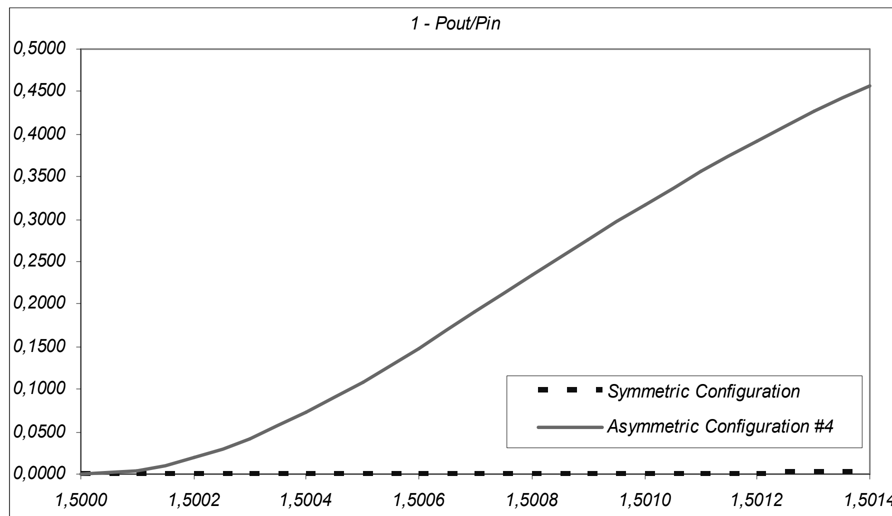

Figure B-3: Comparison of n_{out} dependences of symmetric and asymmetric configurations.

As far as the wavelength dependence of the critical coupling is concerned, the simulations and the calculations present the following wavelength characteristics, where the plot shows the wavelength spectrum of the device for both when the outer layer refractive index equals 1.5000 and 1.5014:

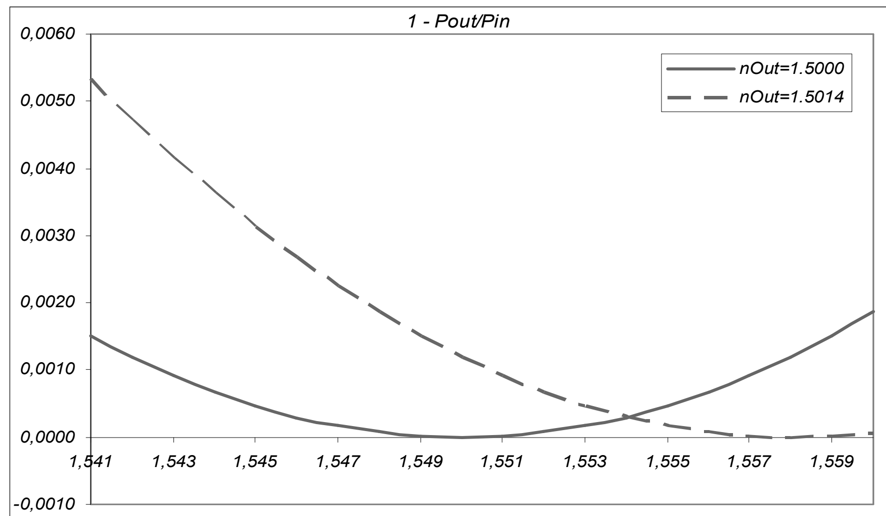

Figure B-4: Output power vs. wavelength of operation for symmetric configuration for n_{out} = 1.5000 and n_{out} =1.5014.

The figure depicts the poor wavelength selectivity of the symmetric structure; for the best case, when the wavelength of operation is shifted an amount of 10 nm, the difference in the output power level is less than 0.01%. Moreover, for the outer layer refractive index of n_{out} = 1.5000, when the multiple wavelength spectrum characteristics of the symmetric and the asymmetric structures are illustrated on the same figure, we obtain the plot shown below, and once again observe that the output power level for the symmetric configuration is totally ignorable compared to that of the asymmetric configuration:

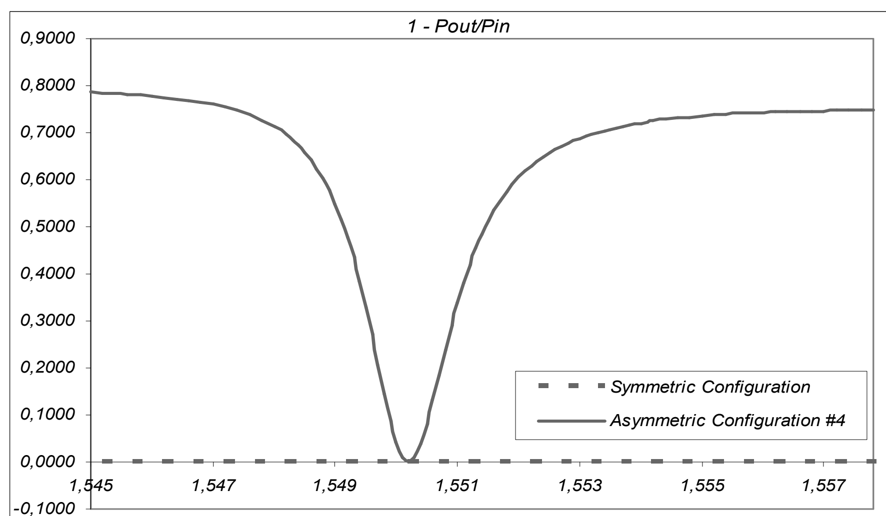

Figure B-5: Comparison of multi-wavelength spectrums of symmetric and asymmetric configurations.

REFERENCES

[1] Toan, N.N., et al. *Sol-gel prepared silica-based materials for sensors and optoelectronic applications*. in *Optoelectronic and Microelectronic Materials and Devices, 2000. COMMAD 2000. Proceedings Conference on*. 2000.

[2] Seiyama, T., et al., *A New Detector for Gaseous Components Using Semiconductive Thin Films.* Analytical Chemistry, 1962. **34**(11): p. 1502-1503.

[3] Lundstrom, I., et al., *A hydrogen - sensitive MOS field - effect transistor.* Applied Physics Letters, 1975. **26**(2): p. 55-57.

[4] Lundstrom, I., et al., *Sensors and Sensory Systems for an Electronic Nose.* NATO ASI Series, 1992. **E 212**: p. 303-319.

[5] Nagle, H.T., R. Gutierrez-Osuna, and S.S. Schiffman, *The how and why of electronic noses.* Spectrum, IEEE, 1998. **35**(9): p. 22-31.

[6] Ferrari, M., et al. *In-liquid sensing of chemical compounds by QCM sensors coupled with high-accuracy ACC oscillator*. in *Instrumentation and Measurement Technology Conference, 2004. IMTC 04. Proceedings of the 21st IEEE*. 2004.

[7] Di Nucci, C., et al., *A measurement system for odor classification based on the dynamic response of QCM sensors.* Instrumentation and Measurement, IEEE Transactions on, 2003. **52**(4): p. 1079-1086.

[8] Nomura, T., A. Saitoh, and S. Furukawa. *Multi-channel chemical sensor using surface acoustic wave device*. in *Ultrasonics Symposium, 1997. Proceedings., 1997 IEEE*. 1997.

[9] Clifford, K.H., et al., *Overview of Sensors and Needs for Environmental Monitoring.* Sensors, 2005. **5**: p. 4-27.

[10] Agrawal, G.P., *Fiber-Optic Communication Systems*. 3 ed. Microwave and Optical Engineering, ed. K. Chang. 2002, New York: John Wiley & Sons, Inc.

[11] Bürck, J., et al., *Fiber-optic evanescent wave sensor for in situ determination of non-polar organic compounds in water.* Sensors and Actuators B, 1994. **18**(1-3): p. 291-195.

[12] Yu, S.-H., C.-H. Chen, and H.K. Chiang. *Fiber optic evanescent wave biosensor for biomolecular detection*. in *Biophotonics, 2004. APBP 2004. The Second Asian and Pacific Rim Symposium on*. 2004.

[13] Shah, R., M. Gold, and R.M. Schaffer. *Development of a fiber optic oxygen and glucose sensor*. in *Engineering in Medicine and Biology Society, 1988. Proceedings of the Annual International Conference of the IEEE*. 1988.

[14] Wilson, D.M., et al., *Chemical sensors for portable, handheld field instruments.* Sensors Journal, IEEE, 2001. **1**(4): p. 256-274.

[15] Harris, R.D., et al. *Integrated optical surface plasmon resonance biosensor for pesticide analysis*. in *Optical Techniques for Environmental Monitoring, IEE Colloquium on*. 1995.

[16] Ho, H.P., et al. *Application of differential phase measurement technique to surface plasmon resonance imaging sensors*. in *Electron Devices Meeting, 2002. Proceedings. 2002 IEEE Hong Kong*. 2002.

[17] Ballantine, D.S. and H. Wohltjen, *Optical Waveguide Humidity Detector.* Analytical Chemistry, Nov. 1986. **58**(13): p. 2883-2885.

[18] Helmers, H., P. Bettech, and R. Rimet, *Integrated optical components employing slab waveguides for sensor applications.* Photonics Technology Letters, IEEE, 1996. **8**(1): p. 81-83.

[19] Pandraud, G. and O. Parriaux, *Zero dispersion in step index slab waveguides.* Lightwave Technology, Journal of, 1999. **17**(11): p. 2336-2341.

[20] Doyle, A. and B.D. MacCraith. *Optical Waveguide Chemical Sensors Using Grating Coupling*. in *Lasers and Electro-Optics Europe, 1998. 1998 CLEO/Europe. Conference on*. 1998.

[21] Nabok, A.V., S. Haron, and A.K. Ray. *Planar silicon nitride waveguides for biosensing*. in *IEE Proc-Nanobiotechnol.* 2003.

[22] Bernini, R., et al. *Planar antiresonant reflecting optical waveguides as sensors for liquid substances*. in *Sensors, 2002. Proceedings of IEEE*. 2002.

[23] Bernini, R., S. Campopiano, and L. Zeni, *Silicon micromachined hollow optical waveguides for sensing applications.* Selected Topics in Quantum Electronics, IEEE Journal of, 2002. **8**(1): p. 106-110.

[24] Okamoto, K., *Fundamentals of Optical Waveguides*. English language ed. Optics and Photonics. 2000, London: Academic Press.

[25] Coldren, L.A. and S.W. Corzine, *Diode Lazers and Photonic Integrated Circuits*. 1995, New York: John Wiley and Sons Inc.

[26] Yariv, A., *Optical Electronics in Modern Communication*. 5 ed. 1997, New York: Oxford University Press.

[27] Ozturk, C., et al., *Filtering characteristics of hybrid integrated polymer and compound semiconductor waveguides.* Lightwave Technology, Journal of, 2002. **20**(8): p. 1530-1536.

[28] Marcatili, E., *Slab-Coupled Waveguides.* Bell System Technical Journal, 1974. **53**: p. 645-673.

[29] Ohtaka, M., M. Matsuhara, and N. Kumagai, *Analysis of the Guided Modes in Slab-Coupled Waveguides Using a Variational Method.* IEEE J. Quantum Electron., 1976. **QE-12**: p. 378-382.

[30] Alferness, R.C. and P.S. Cross, *Filter Characteristics of Codirectionally Coupled Waveguides with Weighted Coupling.* IEEE J. Quantum Electron., Nov 1978. **QE-14**: p. 843-847.

[31] Ozturk, C. and N. Dagli. *Coupled Polymer and Substrate Removed GaAs Waveguides as Tunable Filters*. in *OSA/IPR Trends in Optics and Photonics Conf.* Jul. 2000. Washington DC, USA.

[32] Liu, Y., P. Hering, and M.O. Scully, *An integrated optical sensor for measuring glucose concentration.* Applied Physics B: Lasers and Optics (Historical Archive), 1992. **54**(1): p. 18-23.

[33] Borges, B.-H.V. and L.E.M. de Barros, Jr. *Design of optical biosensor using polymeric waveguide*. in *Microwave and Optoelectronics Conference, 1999. SBMO/IEEE MTT-S, APS and LEOS - IMOC '99. International*. 1999.

[34] *Processing Procedures for Cyclotene 3000 Series Dry Etch Resins*. Rev: Feb. 2005, DOW Chemical Technical Data Sheet.

[35] Huo, X., K.J. Chen, and P.C.H. Chan, *Silicon-Based High-Q Inductors Incorporating Electroplated Copper and Low-K BCB Dielectric.* IEEE Electron Device Lett., Sep. 2002. **23**: p. 520-522.

[36] Chinoy, P.B. and J. Tajadod, *Processing and Microwave Characterization of Multilevel Interconnects Using Benzocyclobutene Dielectric.* IEEE Trans. Comp., Hybrids, Manuf. Technol., Nov. 1993. **16**: p. 714-719.

[37] Johnson, R.W., et al. *Thin-Film Silicon Multichip Technology*. in *Proc. 38th Electron. Comp. Conf.* May 1988. Los Angeles, CA.

[38] Lor, K.P., Q. Liu, and K.S. Chiang, *UV-Written Long-Period Gratings on Polymer Waveguides.* IEEE Photonics Technol. Lett., Mar. 2005. **17**: p. 594-596.

[39] Shin, J., et al., *Novel T-Rail Electrodes for Substrate Removed Low-Voltage High-Speed GaAs/AlGaAs Electrooptic Modulators.* IEEE Trans. Microwave Theory Tech., Feb. 2005. **53**: p. 636-643.

[40] Ericson, T., et al. *Precision passive alignment technologies for low cost array FTTH component*. in *IEEE/LEOS Int. Conf. Optical MEMS*. 2000. Kauai, HI.

[41] Sakamoto, S.R., et al., *Low-Loss Substrate-Removed (SURE) Optical Waveguides in GaAs-AlGaAs Epitaxial Layers Embedded in Organic Polymers.* IEEE Photonics Technol. Lett., 1998. **10**: p. 985-987.

[42] Kane, C.F. and R.R. Krchnavek, *Benzocyclobutene Optical Waveguides.* IEEE Photonics Technol. Lett., 1995. **7**: p. 535-537.

[43] *Processing Procedures for CYCLOTENE 4000 Series Photo BCB Resins (Puddle Develop Process)*. Rev: Feb. 2005, DOW Chemical Technical Data Sheet.

[44] Ozturk, C., *Tunable Hybrid Polymer-Compound Semiconductor Devices for WDM Applications*, in *Department of Electrical and Computer Engineering*. March 2002, University of California Santa Barbara: CA.

[45] Strandjord, A.J.G., et al. *MCM-D fabrication with photosensitive benzocyclobutene: (Processing, solder bumping, systems assembly, and testing)*. in *Proc. SPIE Int. Symp. Microelectronics*. 1995. Los Angeles, CA.

[46] Tacito, R.D. and C. Steinbrüchel, *Patterning of Benzocyclobutene by Reactive Ion Etching.* J. Electrochem. Soc., 1996. **143**: p. 2695-2697.

[47] Chinoy, P.B., *Reactive Ion Etching of Benzocyclobutene Polymer Films.* IEEE Trans. Comp., Hybrids, Manuf. Technol.-Part C, 1997. **20**: p. 199-206.